

# A hyperspectral and multi-angular synthetic dataset for algorithm development in waters of varying trophic levels and optical complexity

Jaime Pitarch<sup>1</sup>, Vittorio Ernesto Brando<sup>1,2</sup>

5 <sup>1</sup>Consiglio Nazionale delle Ricerche (CNR), Istituto di Scienze Marine (ISMAR), Via Fosso del Cavaliere 100, 00133 Rome, Italy

<sup>2</sup>Commonwealth Scientific and Industrial Research Organisation (CSIRO), Environment, Canberra, Australia

*Correspondence to:* Jaime Pitarch (jaime.pitarch@cnr.it)

10 **Abstract.** This data paper outlines the development and the structure of a new synthetic dataset (~~SD~~) ~~within the~~forwithin an extended optical domain, encompassing inherent and apparent optical properties (IOPs-AOPs) alongside associated optically active constituents (OACs). ~~The bio~~Bio-optical modeling benefited from knowledge and data accumulated over the past three decades, ~~resulting on a comprehensive dataset of in situ IOPs, including diverse water typologies, and~~ enabling the imposition of rigorous quality standards and the definition of novel. ~~Consequently, the~~ bio-optical relationships ~~delineated herein that represent are valuable significant contributions to the field on their own.~~

15 Employing the Hydrolight scalar radiative transfer equation solver, ~~we generated~~ above-surface and submarine light fields across the specified spectral range at a “true” hyperspectral resolution (1 nm), covering the ultraviolet down to 350 nm between 350 nm and 800 nm at 1 nm steps were generated,  
20 ~~therefore~~ facilitating algorithm development and assessment for present and forthcoming hyperspectral satellite missions. A condensed-smaller version of the dataset tailored, delivered to twelve Sentinel-3 OLCI bands (400 nm to 753 nm), was crafted also produced, targeting multispectral sensor algorithm research. Derived AOPs encompass an array of above- and below-surface reflectances, diffuse attenuation coefficients, ~~and~~ average cosines and the Q-factor.

25 The dataset is distributed in 5000 files, each file encapsulating a specific IOP scenario, ensuring sufficient data volume for each represented water type represented. A unique feature of our dataset lies in the calculation of AOPs are resolved across the complete range of solar and viewing zenith and azimuthal

**Commented [JP1]:** In response to Reviewer's 1 request (actually we mistakenly understood the comment differently, so please ignore the rebuttal to this)

angles as per the Hydrolight default quadrants, amounting to 1300 angular combinations. This comprehensive directional coverage caters to studies investigating signal directionality, previously  
30 lacking sufficient reference data. The dataset is publicly available for anonymous retrieval via the FAIR repository Zenodo at <https://doi.org/10.5281/zenodo.11637178> (Pitarch and Brando, 2024).

## 1. Introduction and review

### 1.1 Background

Marine optics studies the light ~~that is~~ measured by ~~an~~ optical radiometers, whether ~~installed~~ in the water  
35 or above the surface. The optical signal is conveniently formulated in terms of apparent optical properties (AOPs), which are normalized quantities, less dependent on the intensity of the incident light than the radiances or irradiances from which they originate. The most notable AOP is the remote-sensing reflectance ( $R_{rs}$ ), defined as the water-leaving radiance ( $L_w$ ) per unit of above-water planar downwelling irradiance ( $E_s$ ), ~~and retrievable from satellite observations after atmospheric correction~~. Other quantities  
40 like diffuse attenuation coefficients ~~and~~, average cosines ~~and the Q-factor~~ find applications in marine optics ~~too~~ (Mobley, 1994).

AOPs are ~~used-linked~~ to ~~retrieve~~ the ~~concentrations-of~~ optically active water constituents (OACs),  
~~commonly~~. Such OACs have historically been marine phytoplankton and other suspended and dissolved  
substances. Phytoplankton is typically quantified in terms of ~~the the~~ chlorophyll concentration (C) ~~—A~~  
45 ~~and the other non-living materials-solids~~ suspended in the water can be grouped in the non-algal particles (NAP), quantified by their concentration (N), ~~though different splits of the particulate material are possible, such as particles of organic and inorganic origin, for example~~. Dissolved substances, ~~optically categorized as colored dissolved organic matter (CDOM)~~, are not commonly given in terms of mass concentration units, but in terms of the absorption coefficient spectrum, commonly at 440 nm (Y, or  
50  $a_g(440)$ ).

~~It is possible to develop e~~Empirical algorithms ~~can be developed~~ to invert any of the OACs from measured AOPs by ~~developing-finding~~ statistical relationships ~~from-between~~ matched AOP and OAC data (IOCCG, 2006). This approach, although sometimes operationally robust and mechanistically meaningful, hampers

progress in understanding the optical influence of OACs, which is given by the inherent optical properties  
55 (IOPs), namely the absorption and scattering coefficients. ~~As such, the~~ IOPs can be mathematically  
linked to the OACs with the so-called bio-optical relationships, and to the AOPs through the radiative  
transfer equation, therefore hence being a mathematical bridge between the AOPs and the OACs (Mobley,  
1994).

The OACs are the independent variables that drive the generation of a synthetic dataset (SD). They can  
60 be a single quantity like C (IOCCG, 2006;Loisel et al., 2023), typically chosen for open sea conditions,  
or or, alternatively, a triplet formed by C, N and Y (Nechad et al., 2015) or other combination. ~~The first  
case is typically chosen for open sea conditions, whereas the second is the~~ usually the choice for optically  
complex waters.

More variables give more flexibility but bio-optical relationships must be established for all of them to  
65 derive the ~~In either case, relationships between the IOPs and the OACs must be set to model the radiant  
field, relationships between the IOPs and the OACs must be set.~~ Statistical Rrelationships between C and  
IOPs have been ~~already~~ studied for decades (Bricaud et al., 1998;Loisel and Morel, 1998;Morel and  
Maritorena, 2001). Much less is known about N and Y, and in particular, in optically complex waters,  
where ~~there is no known relationship between the OACs, but also with the additional problem that~~ their  
70 bio-optical properties are much more regionally variable. Nevertheless, in the last two decades, fractional  
information there are notable bio-optical studies in Australian waters (Blondeau-Patissier et al.,  
2009;Cherukuru et al., 2016;Blondeau-Patissier et al., 2017), European waters (Tilstone et al.,  
2012;Martinez-Vicente et al., 2010;Astoreca et al., 2012), South-African lakes (Matthews and Bernard,  
2013) and North-American coastal waters (Aurin et al., 2010;Le et al., 2013;Le et al., 2015), and other  
75 localized areas, have contributed to a significant increase in the understanding of the bio-optics in  
optically complex waters.

Assuming an unpolarized submarine light field, IOPs consist of the wavelength ( $\lambda$ )-dependent absorption  
coefficient ( $a$ ) and the volume scattering function (VSF; symbol  $\beta$ ), which can be broken down to the  
contribution of the single OACs. For the setup used in this SD, consisting of phytoplankton, NAP and  
80 dissolved matter, the IOPs break down as in eq. (1), which includes the contribution by seawater itself  
and assumes that dissolved material does not significantly scatter light in the optical domain:

$$\begin{cases} a(\lambda) = a_w(\lambda) + a_{ph}(\lambda) + a_{NAP}(\lambda) + a_g(\lambda) \\ \beta(\Psi, \lambda) = \beta_w(\Psi, \lambda) + \beta_{ph}(\Psi, \lambda) + \beta_{NAP}(\Psi, \lambda) \end{cases} \quad (1)$$

This breakdown in eq. (1) also assumes that that dissolved material does not significantly scatter light in the optical domain. One can note that, for radiative transfer purposes, it is the total absorption coefficient  $a$  the relevant quantity. Instead, scattering, described by  $\beta$ , the VSF is resolved as a function of the scattering angle ( $\Psi$ ). This creates a varying balance of the single contributors to scattering as their respective variabilities with  $\Psi$  are different. Specifically, the main distinction strongest differences are regards between water and the other particulate materials.

Because of the technical difficulties in measuring angularly-resolved scattering, most commonly, optical theory deals with angular integrals of the VSF, that are much more commonly measured with commercial instrumentation. If the VSF is integrated across the backward hemisphere, one obtains the backscattering coefficient ( $b_b$ ), whereas if one integrates across all directions, one obtains the scattering coefficient ( $b$ ). The total light attenuation along a direction is quantified with the beam attenuation coefficient ( $c = a + b$ ).  $c$  is arguably the most measured IOP in all optics history and its bio-optics has been studied for many decades, as opposed to  $b$  and especially  $b_b$ , whose measurements are much scarcer and more recent.  $c$  keeping the same additive property for each constituent, as shown in hence eq. (2):

$$\begin{cases} b_b(\lambda) = b_{bw}(\lambda) + b_{b,ph}(\lambda) + b_{b,NAP}(\lambda) \\ b(\lambda) = b_w(\lambda) + b_{ph}(\lambda) + b_{NAP}(\lambda) \\ c(\lambda) = c_w(\lambda) + c_{ph}(\lambda) + c_{NAP}(\lambda) + a_g(\lambda) \end{cases} \quad (2)$$

Given a certain constituent, whether phytoplankton or NAP, its VSF is normalized by its scattering coefficient to obtain the phase function (PF) as in eq. (3):

$$\tilde{\beta}_x = \frac{\beta_x}{b_x}, x = ph \text{ or } NAP \quad (3)$$

As shown by eq. (3), this normalization removes the variation of scale due to particle concentration so that the PF is a specific characteristic of the given particle type. For radiative transfer calculations, the PF must be set a priori for each OAC. That can be a measured phase function (He et al., 2017), but more commonly from a family of simulated functions after electromagnetic scattering calculations (Morel et al., 2002; Fournier and Forand, 1994). In particular for the later case, Mobley et al. (2002) arranged an

mathematical equation to select one PF from the whole-Fournier-Forand PF family based on given the backscattering ratio, defined as in eq. (4):

$$B_x = \frac{b_{b,x}}{b_x}, x = ph \text{ or } NAP \quad (4)$$

Despite the fact that the bio-optical modelling for this datasetSD decomposes scattering considers the separate phytoplanktonic and non-algal parts individually, their scattering and attenuation coefficients cannot be measured separately. ~~Only~~ instead, there is literature on bio-optical relationships involving their “particle” aggregates as in eq. (5): ~~can be measured for scattering:~~

$$\begin{cases} b_{dp}(\lambda) = b_{d,ph}(\lambda) + b_{d,NAP}(\lambda) \\ b_p(\lambda) = b_{ph}(\lambda) + b_{NAP}(\lambda) \\ c_p(\lambda) = c_{ph}(\lambda) + c_{NAP}(\lambda) \end{cases} \quad (5)$$

Consideration of particle scattering and backscattering will be needed in a part of the bio-optical modelling, as well as in the comparison to in situ data.

Bulk ~~For~~ absorption and attenuation are also commonly measured, that, after removing the water baselines, become, comparison of model to data is often made for the “non-water” aggregates, which includes the dissolved and particulate contributions components, as in eq. (6):

$$\begin{cases} a_{nw}(\lambda) = a_{ph}(\lambda) + a_{NAP}(\lambda) + a_g(\lambda) \\ c_{nw}(\lambda) = c_{ph}(\lambda) + c_{NAP}(\lambda) + c_g(\lambda) \end{cases} \quad (6)$$

In order to develop ~~new~~-updated bio-optical relationships and remote sensing algorithms, there is a need for large datasets of concomitant OAC-IOP-AOP datasets data across a range of data values, seasons and geographical locations, with fully characterized uncertainties. ~~However,~~ but despite a broader accessibility to field- and laboratory-based IOP instrumentation, ~~current~~ data availability and quality ~~is not~~ are below what was expected twenty-five years ago, when instrumentation became commercially available. Open access OAC-IOP-AOP measurements datasets are scarce, strongly concentrated in some areas and without characterized uncertainties.

Studying the relationships between the IOPs and AOPs allows to build semianalytical models of ocean color: these are simplified algebraic expressions of a desired AOP as a function of the IOPs, and they are

**Commented [JP2]:** This part has been moved here to properly introduce these quantities before use, as requested by Reviewer 1

needed to make retrieval of IOPs from AOPs feasible. Given the absence of publicly available matched IOP-AOP data across a range of water types, and with characterized uncertainties

Given this absence of data, it has been a common choice to develop synthetic datasets (SDs) for optical studies (IOCCG, 2006; Nechad et al., 2015; Loisel et al., 2023). SDs fill the gaps in the data ranges, and their IOP-AOP relationships can be considered error-free, as they are derived from the solution of the radiative transfer equation, yet this exact relationship does not confer validity to the SD per se, as the IOPs resulting from bio-optical modelling could be unrealistic, which has solid physical foundation. SDs have a history of applications to algorithm the development of algorithms of ranging levels of varying complexity, from the semianalytical algorithms (Lee et al., 2002) to a complex neural networks for the MERIS Case 2 water algorithm (Doerffer and Schiller, 2007). If different As such, SDs are very powerful to develop simplified IOP-AOP relationships. In a pioneering work, Gordon et al. (1988) proposed that the underwater irradiance reflectance (R) could be modelled as a second degree polynomial of a parameter "X" that, translating to today's notation, was equivalent to  $\frac{b_{ps}}{a+b_{ps}}$ . They used Monte Carlo modelling to generate a synthetic dataset of matched IOPs and the irradiance reflectance R. This approach has been followed since then by many authors, proposing other analytical expressions and changing the fitted variables, but essentially the approach remains the one by Gordon, with variations. If different sun-view geometries are considered for the output AOPs given an IOP setup, the bidirectional aspects of the AOPs such as the diffuse attenuation coefficient (Lee et al., 2013) or the reflectance can be studied (Morel and Gentili, 1993, 1996; Morel et al., 2002; Park and Ruddick, 2005; Lee et al., 2011) can be studied and analytical models for these variations can be proposed.

New and forthcoming hyperspectral satellite ocean color sensors, such as NASA's PACE or ESA's CHIME are fostering research on Other applications of SDs are related to algorithm development and testing. Matched values of the variable of interest and the input data to be retrieved from (usually an AOP) are used as training data to develop an algorithm. This can be from a simple analytical expression, like the retrieval of non-water absorption at a green band from  $R_{rs}$  in the quasi-analytical algorithm (Lee et al., 2002). At the other end of the algorithm complexity, Doerffer and Schiller (2007) elaborated their MERIS Case 2 water algorithm using an ad-hoc synthetic dataset.

~~Hyperspectral datasets can be used to develop~~ inherently hyperspectral algorithms, that may potentially retrieve additional more information from the oceans than classical multispectral sensors. For this reason, it is considered important then timely to produce a hyperspectral SD, that covers relevant spectral ranges of the aforementioned sensors, for a globally representative range of water types.

~~In the absence of hyperspectral ocean color data, an important application of hyperspectral SDs is to address the question can help to understand of and they are also useful to study~~ how much information is embedded in some key bands of multispectral sensors. In this respect, Talone et al. (2024) used a preliminary version of this SD to propose a hyperspectral  $R_{rs}$  reconstruction scheme from AERONET-OC data, in order to validate satellite derived hyperspectral radiometric products, confirming the validity of the reconstruction in large portions of the visible spectrum with constrained uncertainties.

## 1.2 Existing synthetic datasets

~~The usage of a~~ Numerical models for computing light fields ~~has have~~ been used for common practice for several decades already (Mobley et al., 1993). In a pioneering work, Gordon et al. (1988) proposed that the underwater irradiance reflectance ( $R$ ) could be modelled as a second degree polynomial of a parameter “ $X$ ” that, translating to today’s notation, was equivalent to  $\frac{b_T}{a+b_T}$ . To verify their hypothesis and to calculate the polynomial fit, they used Monte Carlo modelling to generate a synthetic dataset of matched IOPs and the irradiance reflectance  $R$ . This approach has been followed since then by many authors, proposing other analytical expressions and changing the fitted variables, but essentially the approach remains the one by Gordon, with variations. Some ~~researchers authors have~~ developed internal codes (D’Alimonte et al., 2010) while ~~some others have~~ released them to the public (Chami et al., 2015; Rozanov et al., 2014). By far, the most popular code in the marine optics community has been Hydrolight (formerly from Sequoia Scientific, Inc., now from Numerical Optics, Ltd.), which is available upon purchase. Its popularity is due to arises from, on one hand, the convenient data input management ~~of data input~~, which allows the simulation of every possible case study in ocean optics with relative ease, and the data output, which includes the full array of radiometric quantities and AOPs needed. Its prevalence in the field is such that all datasetSDs reviewed in this paper, as well as the one presented here,

were generated with Hydrolight. It is therefore of importance that support and further development of Hydrolight is ensured for the future.

~~Most of previously developed were developed to fit a given investigation and were not released to the public.~~ This article only considers ~~these SDs~~ that were publicly released. Only their main characteristics will be mentioned, especially those relevant ~~for to~~ the new ~~synthetic datasetSD~~ that we are presenting.

### 1.2.1 The IOCCG dataset

The first and the most cited of the ~~datasetSDs~~ in this small review is the IOCCG ~~datasetSD~~ (IOCCG, 2006). The release of this ~~datasetSD~~ came at a time where the study of bio-optical relationships and the development of algorithms was at its all-time ~~peak-high~~ (e.g., Twardowski et al., 2001;Loisel and Morel, 1998;Morel and Maritorena, 2001;Lee et al., 2002). It is a ~~datasetSD~~ for testing and development of in-water algorithms in open and oceanic waters.

~~As such,~~ The single independent variable ~~of the that drives~~ IOP variability is the chlorophyll concentration (C), ~~for concentrations between ranging from 0.03 and to 30 mg m<sup>-3</sup>.~~ ~~Phytoplankton absorption Bbio-optical modelling uses a database of real Pphytoplankton absorption spectra (a<sub>ph</sub>) spectra measured in the field is the only actually measured IOP that is used, coming from a database of in situ absorption spectra (a<sub>ph</sub>).~~ Given a C value, a random a<sub>ph</sub> is chosen within the database, ~~and it is scaled by a factor,~~ so that the scaled a<sub>ph</sub>(440) verifies ~~the an average~~ relationship ~~of the latter~~ to C given by Bricaud et al. (1995), ~~given by~~  $a_{ph}(440) = A(440)C^{E(440)}$ . Notably, the chosen a<sub>ph</sub> belongs to a subset of a<sub>ph</sub> spectra associated to C values within a ~~short-narrow~~ range of the given C. This choice implies assuming that a<sub>ph</sub> spectra that are related to very different concentrations are not only different in magnitude, but also in shape.

The ~~rest of~~ bio-optical relationships are set after (mostly) published relationships, with the addition of some randomness, ~~that tries to model s some the~~ spread around the mean relationship, attributed to natural causes, ~~that are and~~ not captured by these average equations. While that choice is a positive feature of the ~~datasetSD~~, many parameterizations appear arbitrary.

The ~~volume scattering function-VSF~~ is modelled after splitting the particulate matter in phytoplankton and ~~all non-algal (non-pigmented) particles~~ NAP. The former scatters light following a Fournier-Forand



210 phase function of fixed  $B_{ph} = 0.01$ , whereas the latter scatters light according to the average Petzold phase function,  $B_{phNAP} = 0.0183$ . This is identified as a major limitation ~~for this dataset~~, as there are a number of concerns on the Petzold phase function that will be detailed below.

Radiances ~~were generated~~ are available from 400 nm to 800 nm every 10 nm for the nadir view direction, and for two sun zenith angles (0 and 30 °).

### 215 1.2.2 The ~~CoastColour~~ CoastColour dataset

The ~~CoastColour~~ CoastColour ~~synthetic dataset~~ SD (Nechad et al., 2015) was generated in the framework of an ESA project, aimed at the evaluation of algorithms ~~in-for~~ coastal waters. The project included the compilation of large amounts of in situ data, but the patchiness in the geographical and data range distributions and the disparity of measurement techniques, without quantified uncertainties, made evident the need of a synthetic dataset SD that focused in such areas and associated data ranges.

The dataset SD is driven by three OACs: ~~phytoplankton, NAP and CDOM. The non water substances were divided into~~ phytoplankton, “mineral particles” and CDOM. This, in principle, ignores the contribution of non-algal particles of biological origin, but in practice, their “mineral particles” compartment de facto stands for “non-algal particles”. 5000 triplets of their respective concentrations

225 (C,N,Y) were randomly generated. Although not documented in their paper, these three constituents show some degree of linear crossed correlation, ~~which a feature that~~ is seen in in situ datasets when these variables span across a large range. This choice also mechanistically avoids the generation of many unrealistic  $R_{rs}$  spectra coming from unrealistic (C,N,Y) triplets. ~~The OACs are related to the IOPs according to some bio-optical relationships. The non water substances were divided into phytoplankton,~~

230 ~~“mineral particles” and CDOM. This, in principle, ignores the contribution of non algal particles of biological origin, but in practice, their “mineral particles” compartment de facto stands for “non algal particles”~~.

Bio-optical modelling relationships are based on average parameters and regression equations from literature, ~~without randomization strategies to mimic~~ ignoring the natural variability. For example, phytoplankton absorption ~~was-is~~ modelled by simply applying the average “A” and “E” power law coefficients by Bricaud et al. (1995) at 440 nm for a given chlorophyllC, which ~~ignores phytoplankton~~

240 ~~diversity and~~ makes all 5000 modelled  $R_{rs}$  ~~to~~ have the same average pigment features. Furthermore, ~~all~~ spectral slopes as well as the “~~mineral particles~~”-specific absorption and scattering coefficients at reference bands are set constant. Overall, these bio-optical choices create an optical uniformity that results in ~~artificially-fictitiously~~ tight relationships between various IOPs or between IOPs and AOPs, as well as their ratios. ~~This bio-optical modelling can,~~ potentially misleading ~~the~~ users about the performance of any algorithm that is evaluated.

245 Following the IOCCG approach, angular scattering ~~was~~ is modelled by assuming a Fournier-Forand phase function for phytoplankton and the average Petzold phase function for NAP, with fixed backscattering ratios for both.

The datasetSD delivers the absorption coefficient divided in the total non-water component and the phytoplankton absorption. To separate CDOM and NAP absorption, the users need to generate CDOM spectra ~~with from~~ the reported value at a given wavelength and the CDOM spectral slope.

250 ~~Following the IOCCG approach, angular scattering was modelled by assuming a Fournier-Forand phase function for phytoplankton and the average Petzold phase function for NAP, with fixed backscattering ratios for both.~~

AOPs ~~were generated with Hydrolight~~ are given from 350 nm to 900 nm every 5 nm, for the sun zenith angles 0, 40° and 60°, and the single nadir-viewing angle for radiances.

### 255 1.2.3 Loisel’s dataset

Loisel’s datasetSD (Loisel et al., 2023) is mainly characterized by its intention effort to compensate the disproportionate in situ data density from coasts and ~~continental~~-shelves with respect to the open oceans, which ~~instead represent cover~~ a much larger area. ~~According to them, this issues~~ Such disproportion in other datasets may have a biasing effect when ~~synthetic datasets are used to~~ developing optical algorithms based on AOP vs. IOP relationships, especially when the underlying goal is to represent a broad range of IOPs encountered within the global ocean. In this regard, Loisel’s SD benefits from satellite-retrieved IOPs over the global oceans ~~were~~ organized in histograms, ~~which were~~ used as guides to “trim” the

~~histograms of the~~ in situ data histograms, so that the data distributions in the datasetSD ~~would~~ closely match the global ones.

265 Bio-optical modelling follows the IOCCG approach with modifications. IOP variability is driven by chlorophyll concentration only. ~~Bio-optical modelling follows the IOCCG approach with modifications, thus choosing and~~ phytoplankton absorption is taken randomly from a pool of real spectra, and then scaled ~~and giving some randomness to the relationships to mimic the bio-optical variability found in nature (1995).~~ The CDOM and NAP spectral slopes ~~were~~ are given random values within ~~a large wide~~ uniform distributions. ~~This choice is preferable to assigning them a fixed values, although yet which might have been some level of constrain~~ ed with available in situ data pools appeared possible instead. Angular scattering of phytoplankton ~~was~~ is modelled with a fixed Fournier-Forand phase function of  $B_{ph} = 0.01$ . There is, however, evidence (Whitmire et al., 2010) that  $B_{ph}$  varies across an order of magnitude. In Hydrolight,  $B_{ph}$  is used to choose the phase function, which, for a given  $b_{ph}$ , implicitly

270 determines  $b_{b,ph}$  and therefore, the amplitude of the signal. This detail is important when one seeks to replicate relationships of  $b_{bp}$  to other IOPs that are found in measured data.

NAP scattering was ~~is~~ modelled as a spectral power law. Its angular scattering incorporates one innovation respect to the previous datasetSDs by dropping the Petzold phase function and using instead a Fournier-Forand function of  $B_{NAP} = 0.018$ , with such  $B_{NAP}$  close to the average Petzold value, but with a more realistic angular variation that better resembles measured VSFs much more closely (Sullivan and Twardowski, 2009).

Output AOPs are given between the range 350 nm – 750 nm in steps of 5 nm. Several versions of the datasetSD are available for various combinations of inelastic scattering being or not considered. Notably, this datasetSD provides the data output at several depths. Simulations are made for the sun zenith angles

285 0, 30° and 60°, and the single nadir-viewing angle for radiances. All data ~~is~~ are compiled in a single netCDF file for each type of simulation.

### 1.3 Creating a new dataset

The ~~This~~ brief review of existing ~~synthetic dataset~~SDs has identified limitations ~~in bio-optical modeling, emphasizing the critical need for meticulous refinement in order to derive meaningful radiance outputs from radiative transfer simulations. Such issues that~~ can be summarized in:

- (1) Overly simplified bio-optical parameters: spectral slopes, specific absorption or scattering at a reference wavelength, are often set as static values, ~~typically derived from averaging mostly coming from~~ datasets ~~averages~~, thereby masking the optical diversity inherent within them. In this new ~~dataset~~SD, we address this limitation by considering the variability of each optical parameter across available datasets and exploring their ~~prediction-predictability~~ as a function of other parameters.
- (2) An absence of constraints between absorption and scattering ~~for-of~~ a given water ~~constituent (OAC) such as phytoplankton or non algal particles (NAP)~~: it is evident that absorption and scattering ~~of a given AOC should-must~~ exhibit statistical correlations due to their association with the same type of particles, but it ~~seems-is~~ the rule that both properties are modelled independently, potentially resulting in absorption-scattering pairs that do not accurately reflect the characteristics of naturally occurring particles. In this ~~dataset~~SD, we address this issue by leveraging in-situ data to constrain the modeling of both phytoplankton and NAP. This approach ensures that the corresponding absorption-scattering pairs align with all experimental evidence in statistical terms.
- (3) ~~Re-use~~Extrapolation of bio-optical relationships: a published relationship between two quantities is applied to different ones. For example, the average relationship between chlorophyll and particle scattering by Loisel and Morel (1998) has been used to model phytoplankton scattering, which is only a fraction of the total scattering.
- (4) Limited validation of bio-optical models: ~~some statistical relationships are presented without evidence. In situ using accessible in situ data is crucial. With new open access datasets, there arises an-offer an~~ opportunity to assess historical bio-optical relationships while also fostering the development of new ones, ~~and such potential -To our opinion, such data~~ has not been yet fully ~~utilized~~developed.

315 (5) Limited spectral coverage of the blue-UV: in view of present and future satellite missions, it is desirable to generate [datasetSDs](#) that at least cover the range from 350 nm.

320 (6) Limited directional AOP output: published [datasetSDs](#) focus on the nadir viewing direction, for a few sun zenith angles. However, the light field is inherently directional, and ignoring directionality introduces errors in remote sensing algorithms. [In consonance with a renewed impetus of optical studies that address the problem of directionality](#) Here, ~~we~~ it is aimed at generating a fully directional [datasetSD](#), accounting for all possible sun and view geometries, ~~in consonance with a renewed impetus~~ [view of optical studies that address the problem of directionality](#).

## **2. Spectral IOPs data mining and reduction**~~In situ data and bio-optical modelling~~

325 ~~The generation of bio-optical relationships needs support by in situ data, and a high quality is required, to be confident enough that the relationships that are found within the data are neither biased nor spurious. Unfortunately, processing details are often lacking, and data are seldom provided with an uncertainty estimate. It was nevertheless is, however, assumed that the practitioners data providers, based on their experience, followed best practices. Indeed, as most of these data come were collected in the framework of optical studies funded after the funding of projects by space agencies that involve related studies, and we believe that the groups that were involved were confident enough in the quality of the data before sharing. Still, data was selected based on the usage of appropriate instrumentation and processing, when such information was available. Furthermore, selection criteria was rather aggressive, based on shape and fitness indices, overall providing confidence on the final retained data.~~

### **1.4 In situ data**

#### **1.5.1 Phytoplankton absorption**

335 Phytoplankton absorption  $a_{ph}$  ~~is the only IOP that is not modelled as a simple analytical function due to its~~ ~~has a~~-complex spectral shape, which determines the ~~small scale~~ spectral features of ~~derived-related radiometric variable~~ AOPs. For this reason, it is important to select high-quality  $a_{ph}$  data, ~~suitable as input for radiative transfer simulations. Since the purpose of these data is to feed the simulations, they do not need to be geo-referenced nor matched to any other variable. However,~~ ~~For this~~ [datasetSD](#), it was required

340

that  $a_{ph}$  data was ~~collected~~ sampled at or close to the surface of the water column, as bio-optical relationships involving phytoplankton seem to vary depending on the vertical layer (Bricaud et al., 1995;Loisel and Morel, 1998). In terms of spectral range, a condition ~~for data selection~~ was imposed that  ~~$a_{ph}$  data should be given~~ include has to be given at at least the range from 350 nm to 800 nm, which was a quite limiting requirement for the lower limit, as in most cases,  $a_{ph}$  is provided down to 400 nm or 380 nm.

Data were searched from the database SeaBaSS, providing many spectra, though a significant amount of them with anomalous spectral patterns. ~~A first screening of the data identified many noisy and biased spectra. As a first baseline correction, the residual NIR value, which was estimated as the average  $a_{ph}$  between 780 nm and 800 nm, was subtracted.~~ Then, a PANGAEA search ~~was performed. It~~ delivered many excellent spectra instead, collected in seven Polastern cruises (Soppa et al., 2013a;Liu et al., 2019b, c;Bracher, 2019;Bracher et al., 2021k;Bracher et al., 2021f;Bracher and Taylor, 2021), one Sonne cruise (Bracher et al., 2021l) and one Heincke cruise (Bracher et al., 2021c). The PACE dataset (Casey et al., 2020) was also used, in particular by data from the PI Schaeffer and from the Biosope cruise. In this latter case, the spectral range requirement was relaxed, allowing a maximum wavelength coverage of 750 nm, in order to keep some necessary low-end  $a_{ph}$  that were very necessary for their representativity of the lowest  $a_{ph}$  in the world ~~the clearest waters.~~ At the ~~Then, to increase the~~ high end of the range, Dr. A. Castagna's dataset on Belgian coastal and inland waters (Castagna et al., 2022) was used. Their published  $a_{ph}$  was only available until from 380 nm, so Dr. Castagna kindly made reprocessed available the  $a_{ph}$  spectra especially processed for this investigation down to 350 nm especially for this investigation, though expressing some methodological concerns about the data accuracy in the UV. Finally, a new CNR small dataset from a recent cruise (publication in preparation) ~~has was~~ also ~~been~~ included in the global dataset. ~~Data quality among databases varied greatly, from generally poor within SeaBaSS to the carefully produced Castagna's spectra. In terms of selection and processing and selection.~~ As a first baseline correction, the residual NIR value, which was estimated as the average  $a_{ph}$  between 780 nm and 800 nm (between 740 nm and 750 nm for Biosope), was subtracted. Given the high amount of data in total, it was preferred to apply rather aggressive filter selection criteria. Spectra were smoothed with an 11 nm

rectangular moving window to eliminate random noise introduced by the spectro-photometers. A **relative** noise parameter was calculated as the standard deviation of the difference between the unfiltered and the filtered  $a_{ph}$ , divided by a guess of the chlorophyll concentration based on  $a_{ph}(665)$  (~~details below~~) after Bricaud et al. (1995). Spectra were retained if this noise parameter was lower than 0.002, except for the Biosope dataset, where the threshold was **relaxed and** raised **at-to** 0.004 ~~in order to keep some low end  $a_{ph}$  that were very necessary for their representativity of the lowest  $a_{ph}$  in the world.~~ Additionally, the absolute value of the second derivative with respect to the wavelength,  $|a''_{ph}|$ , was calculated as a measure of spectral noise ~~and spectra with~~ The 90<sup>th</sup> percentile of  $|a''_{ph}|$  between 350 nm and 800 nm ~~was stored. Only spectra having this percentile~~ lower than 0.0032 were selected.

Further ~~exclusion-selection~~ criteria were applied based on ~~the~~ spectral shapes. We defined the following indexes:

$$\begin{aligned}
 m_{UV} &= \min\{a_{ph}(\lambda \in [350 \text{ nm}, 450 \text{ nm}])\} \\
 M_{UV} &= \max\{a_{ph}(\lambda \in [350 \text{ nm}, 450 \text{ nm}])\} \\
 M_G &= \max\{a_{ph}(\lambda \in [550 \text{ nm}, 560 \text{ nm}])\} \\
 I_{CHL} &= \max\{a_{ph}(\lambda \in [650 \text{ nm}, 700 \text{ nm}])\} - \min\{a_{ph}(\lambda \in [650 \text{ nm}, 700 \text{ nm}])\}
 \end{aligned} \tag{77}$$

Therefore, the following selection thresholds were applied ~~to the indexes in eq. (7), that-which~~ were chosen based on experience so that clearly anomalous spectra would be discarded yet trying not to penalize natural variability. These were  $m_{UV}/I_{CHL} > 0.1$ ,  $M_{UV}/I_{CHL} < 6$  and  $M_G/M_{CHL} < 2$ . In particular, the thresholds involving the UV discarded many spectra that raised excessively in the UV, likely consequence of insufficient bleaching of the filtered sample, or that tended to zero or even negative values instead. At the green range, it was assumed that the spectrum shall present a valley or at least a value that is not much larger than the chlorophyll peak.

~~Finally, Other than these thresholds,~~ some spectra exhibited secondary peaks very distant from 676 nm, which was likely a sign of spectral misalignment. Therefore, it was required that such peak was between 670 nm and 681 nm for inclusion.

All the filtering procedures led to the selection of 3025 high quality  $a_{ph}$  spectra, representing a very wide range of values and water types.

## 1.5.12.2 CDOM absorption

CDOM absorption at 440 nm ( $a_g(440)$  or  $Y$ ) is one of the three independent variables of the bio-optical modelling. Its value is therefore given. ~~Still, such value needs to be propagated to the whole The full spectrum is covered~~ by assuming a spectral variation, modelled here as the usual exponential shape. The value of the spectral slope  $S_g$  ~~and its potential relation to  $a_g(440)$  must be determined after bio-optical modelling from. For this sake~~; a pool of in situ CDOM absorption spectra ~~were collected~~. CDOM is stored by filtering seawater with 0.2  $\mu\text{m}$  pore size filters. ~~A and~~ absorption is measured through light transmission, as the scattering of the sample can be considered negligible. The most common measurement instrument is a bench spectrophotometer, where water is poured in a cuvette of a given path length, usually between 1 cm and 10 cm. In clear waters, because of the short path length that makes resulting data very noisy, a liquid waveguide capillary cell (LWCC) system like UltraPath™ (World Precision Instruments, Inc.) is preferred, ~~as they allow~~ ~~has a~~ much larger path lengths, up to 2 m, therefore obtaining proper optical densities for a given sample, even in the clearest waters. In this article, only open access CDOM data measured with UltraPath were selected in open ocean waters, whereas in complex coastal and inland waters, cuvette-based measurements were accepted as well. Therefore, the pooled CDOM data ~~consists~~ ~~consisted~~ of the PACE datasets Schaeffer, Biosope and Mouw, Castagna's measurements, as well as a large PANGAEA dataset based on several Polarstern cruises (Bracher et al., 2021a; Bracher et al., 2021b; Bracher et al., 2021i; Bracher et al., 2021h) and some smaller campaigns in coastal areas (Juhls et al., 2019; Hölemann et al., 2020; Bracher et al., 2021g; Pykäri, 2022). In all cases, data had to be provided at the range from 350 nm to 750 nm and close to the surface.

CDOM spectra were fitted to a decreasing exponential function with a given offset,  $\hat{a}_{g,mod} = a_g(\lambda_0)e^{-S_g(\lambda-\lambda_0)} + a_{g,off}$  using non-linear least squares, with a bi-square weighting function to minimize the effect of outliers. ~~Then, the offset was removed:  $\hat{a}_{g,mod} = \hat{a}_{g,mod} - a_{g,off}$ .~~ Notably, fits were made in linear scale, as making them in logarithmic scale would artificially raise the weight of spectral regions where CDOM is less relevant. ~~Fits were required that~~ ~~An excellent fit between model and data was required~~ ( $r^2 > 0.995$ ), to exclude ~~eventual anomalous~~ shapes ~~that did not verify the exponential~~

Formatted: Heading 2



420 assumption. Then, finally, the offset was removed:  $a_{g,mod} = \hat{a}_{g,mod} - a_{g,off}$ . In total, The result of this procedure was 1168 ( $a_g(\lambda_0), S_g$ ) spectra were retained pairs.

### 1.5.2.3 NAP absorption

As with CDOM, NAP absorption spectra ( $a_{NAP}$ ) are not introduced directly in the radiative transfer simulations but modelled as exponential functions. Data selection again prioritized high-quality as the data quantity was sufficient to derive the statistical relationships. Here, a PANGAEA search delivered data from various Polarstern cruises (Gonçalves-Araujo et al., 2018; Liu et al., 2019a, d; Wiegmann et al., 2019; Bracher et al., 2021j; Bracher et al., 2021e, d; Bracher and Liu, 2021; Soppa et al., 2013a, b) and one Heincke cruise (Bracher et al., 2021d). From the PACE database,  $a_{NAP}$  from the cruise Biosope and the PIs Mouw and Schaeffer was were included. Castagna's measurements were also included, as well as recent CNR data.

430 As for CDOM, an exponential shape was fitted,  $\hat{a}_{NAP,mod} = a_{NAP}(\lambda_0)e^{-S_{NAP}(\lambda-\lambda_0)} + a_{NAP,off}$  in linear scale, and then the offset was removed,  ~~$a_{NAP,mod} = \hat{a}_{NAP,mod} - a_{NAP,off}$~~ . ~~And~~ the condition  $r^2 \geq 0.995$  was imposed, ~~and then~~ The offset was removed thereafter,  $a_{NAP,mod} = \hat{a}_{NAP,mod} - a_{NAP,off}$ . still recognizing that at least a part of  $a_{NAP,off}$  this offset might be physically realistic and not only due to residual scatter errors. In such a case, it would be needed to seek pursue bio-optical relationships between  $a_{NAP,off}$  the offset and other variables, in order to generate its value for the dataset. In the absence of sufficient knowledge, we adopted the classical approach of removing the offset, as previous datasetSDs (IOCCG, 2006; Nechad et al., 2015; Loisel et al., 2023). The result of this procedure was 1349 ( $a_{NAP}(\lambda_0), S_{NAP}$ ) pairs, leading to a total of 1349 valid spectra.

### 1.5.3.4 CSIRO's dataset Particle backscattering

440 In situ particle backscattering  $b_{bp}$  is not a Hydrolight input parameter in the configuration that was used, but it was needed for the determination of the bio optical relationships of the particulate fraction, as it will be detailed below. In addition, it is desirable to collect a comprehensive dataset of  $b_{bp}$  matched to

Formatted: Heading 2

Commented [JP3]: In response to reviewer 1

Formatted: Heading 2

fractionated absorption components to check the consistency of crossed relationships in the synthetic dataset respect to those found in natural waters.

Specifically,  $b_{pp}$  at 440 nm or near wavelength was searched. The availability of such data is very limited and the quality is essentially unknown. Here, a best effort exercise was made by collecting all available data, of an open source or not. These were found from NOMAD (Werdell and Bailey, 2005), the PACE datasets Biosope and from the PI Mouw (Casey et al., 2020), and from Castagna's dataset (Castagna et al., 2022). In this latter case,  $b_{pp}$  was not available, but since such data are considering especially important for their very high values,  $b_{pp}$  was inferred through semi-analytic closure from absorption and  $R_{rs}$  (Lee et al., 2011). Finally, data collected in Australian waters by CSIRO researchers (Blondeau-Patissier et al., 2009; Blondeau-Patissier et al., 2017; Cherukuru et al., 2016; Oubelkheir et al., 2023; Brando et al., 2012) was also included here. CSIRO's dataset contains several IOPs and OACs at reference wavelengths, that were used to develop some of the bio-optical relationships that were used to produce the synthetic dataset. In what regards Particlesuch as  $a_{ph}(440)$ ,  $a_{NAP}(440)$ ,  $a_g(440)$ , backscattering specifically,  $b_{pp}(555)$ , is only provided at the reference wavelength 555 nm and with an estimated of its spectral slope ( $\eta$ ). Also, the chlorophyll concentration ( $C$ ) and the total suspended matter concentration ( $T$ ) contained in the dataset. For this specific dataset, the slope was not only used to shift  $b_{pp}$  from 555 nm to 440 nm, but also for a part of the bio-optical modelling, detailed below. Importantly, specific NAP absorption at 440 nm,  $a_{NAP}^*(\lambda_0) = \frac{a_{NAP}(\lambda_0)}{N}$ . For this specific dataset, the slope was not only used to shift  $b_{pp}$  is also provided, alongside with the chlorophyll and NAP concentrations, overall making this dataset unique for advanced bio-optical modelling. For this specific dataset, the slope was not only used to shift  $b_{pp}$  from 555 nm to 440 nm, but also for a part of the bio-optical modelling, detailed below.

### 1.6.3. Bio-optical modelling

Assuming an unpolarized submarine light field, IOPs consist of the absorption coefficient and the volume scattering function (VSF; symbol  $\beta$ ), which can be broken down to the contribution of the single OAC:

Formatted: Heading 1

$$\left\{ \begin{array}{l} \alpha(\lambda) = \alpha_w(\lambda) + \alpha_{ph}(\lambda) + \alpha_{NAP}(\lambda) + \alpha_g(\lambda) \\ \beta(\Psi, \lambda) = \beta_w(\Psi, \lambda) + \beta_{ph}(\Psi, \lambda) + \beta_{NAP}(\Psi, \lambda) \end{array} \right. \quad (2)$$

This formulation implies the assumption that dissolved material does not significantly scatter light in the optical domain.

Commonly, optical theory deals with angular integrals of the VSF. If it is integrated across all directions, one obtains the scattering coefficient, whereas if one integrates across the backward hemisphere, one obtains the backscattering coefficient:

$$\left\{ \begin{array}{l} b(\lambda) = b_w(\lambda) + b_{ph}(\lambda) + b_{NAP}(\lambda) \\ b_b(\lambda) = b_{bw}(\lambda) + b_{b,ph}(\lambda) + b_{b,NAP}(\lambda) \end{array} \right. \quad (3)$$

Given a certain constituent, whether phytoplankton or NAP, its VSF is normalized by its scattering to obtain the phase function (PF):

$$\tilde{p}_x = \frac{p_x}{b_x}, x = ph \text{ or } NAP \quad (4)$$

It can be a measured phase function (He et al., 2017), but more commonly from a family of simulated functions after electromagnetic scattering calculations. (!!! INVALID CITATION !!! (Morel et al.,

2002;Fournier and Forand, 1994);2002)

For radiative transfer calculations, the PF must be a priori established for each OAC. The backscattering ratio is used to constraint the PF to a first order (Mobley et al., 2002):

$$B_x = \frac{b_{b,x}}{b_x}, x = ph \text{ or } NAP \quad (5)$$

With this information, a phase function must be assigned to each type of particle, consistent with the given data, such as  $B_x$ . It can be a measured phase function (He et al., 2017), but more commonly from a family of simulated functions after electromagnetic scattering calculations (Morel et al., 2002;Fournier and Forand, 1994)

Despite being the bio-optical modelling more accurate if the particulate material is decomposed into the phytoplanktonic and the non-phytoplanktonic parts (some discussion below), scattering meters do not

measure the separate contributions of phytoplankton and NAP. Instead, their “particle” aggregates are measured:

$$\left\{ \begin{array}{l} b_p(\lambda) = b_{ph}(\lambda) + b_{NAP}(\lambda) \\ b_{bp}(\lambda) = b_{b,ph}(\lambda) + b_{b,NAP}(\lambda) \end{array} \right. \quad (6)$$

This aggregation is therefore made when the bio-optical modelling of scattering is about to be evaluated against in situ data.

The bio-optical modelling of the various terms of the absorption and scattering budgets will be modelled as a function of the OACs will be explained with high detail in the following sub-sections. Readers interested in a comprehensive summary can find all sequential steps summarized as detailed in the next sections and summarized in Table 1.

**Table 1 Summary of the bio-optical modelling**

$a_{ph}(\lambda)$	$a_{ph}(\lambda)$ from a quality-controlled database, adjusted by a factor to verify $a_{ph}(670) = A(670)C^{E(670)}$ , $A(670) = 0.019093$ , $E(670) = 0.95568$ ; <del><math>A(670) = 0.019093</math>, <math>E(670) = 0.95568</math></del>
$c_{ph}(\lambda)$ <del><math>\tilde{\beta}_{ph} \hat{\beta}_{pp}(\Psi)</math></del>	$c_{ph}(\lambda) = c_{ph}(660) \left( \frac{660}{\lambda} \right)^{n_1}$ $n_1 = -0.4 + \frac{1.6 + 1.2\Re}{1 + C^{0.5}}$ $\Re \leftarrow \mathcal{U}(0,1)$ <del><math display="block">\tilde{\beta}_{ph} \hat{\beta}_{pp}(\Psi) \sim FF(B_{ph})</math></del> $B_{ph} \leftarrow \mathcal{NN}(\mu, \sigma)$ $\mu = 0.002 + (0.01 - 0.002) \cdot \exp[-0.56 \log_{10}(C)]$ $\sigma = 0.001(3 - \log_{10}(C)) + 0.001$
$a_{NAP}(\lambda)$	$a_{NAP}(\lambda) = N a_{NAP}^*(440) \cdot e^{-S_{NAP}(\lambda-440)}$ $\log_{10} a_{NAP}^*(440) \leftarrow \mathcal{NN}(\mu, \sigma)$ $\mu = a e^{(b \log_{10} \frac{C}{N} + c)}$ $a = -0.1886, b = -1.055, c = -1.27$ $\sigma = 0.2627$

	$S_{NAP}$ $\leftarrow \begin{cases} \mathcal{U}(0.01, 0.035) & \text{if } a_{NAP}(440) < 4 \cdot 10^{-4} \text{ m}^{-1} \\ \text{Ln } \mathcal{N}(-0.308x - 5.101, -0.0558x + 0.1164) & \text{if } a_{NAP}(440) \in [4 \cdot 10^{-4}, 0.06] \text{ m}^{-1} \\ \mathcal{N}(0.011, 0.016) & \text{if } a_{NAP}(440) \geq 0.06 \text{ m}^{-1} \end{cases}$
$c_{NAP}(\lambda),$ <del><math>\tilde{\beta}_{NAP} \hat{\beta}_{NAP}</math></del>	$c_{NAP}(\lambda) = c_{NAP}(440) \left( \frac{\lambda}{440} \right)^{-\gamma_{NAP}}$ $\gamma_{NAP} \leftarrow \mathcal{N}(\mu, \sigma)$ $\mu = 0.7, \sigma = 0.3$ $c(440) = a_{NAP}(440) + b_{NAP}(440)$ $b_{NAP}(440) = \frac{b_{b,NAP}(440)}{B_{NAP}}$ $B_{NAP} \leftarrow \mathcal{U}(0.01, 0.02)$ $b_{b,NAP}(440) = T b_{bp}(440) - b_{ph}(440)$ $T = N + 0.07C$ $b_{bp}^*(440) = b_{bp}^*(555) \left( \frac{440}{555} \right)^{-\eta}$ $\eta \leftarrow \text{Burr}(\alpha, c, k)$ $\alpha = 0.854, c = 4.586, k = 1.108$ $\log_{10} b_{bp}^*(555) \leftarrow \mathcal{N}(\mu, \sigma)$ $\mu = m \log_{10} a_{NAP}^*(440) + n$ $m = 0.6834, n = -0.9483$ $\sigma = 0.2627$ <del><math display="block">\tilde{\beta}_{NAP} \hat{\beta}_{NAP}(\Psi) \sim FF(B_{NAP})</math></del>
$a_g(\lambda)$	$a_g(\lambda) = Y e^{-S_g(\lambda-440)}$

$S_g$	$\leftarrow \begin{cases} \mathcal{U}\mathcal{H}(0.01,0.025) & \text{if } a_g(440) < 0.02 \text{ m}^{-1} \\ \mathcal{N}\mathcal{N}(-0.00040161x + 0.017508, -0.0003012x + 0.001881) & \text{if } a_g(440) \in [0.02,5) \text{ m}^{-1} \\ \mathcal{U}\mathcal{H}(0.0143,0.017) & \text{if } a_g(440) \geq 5 \text{ m}^{-1} \end{cases}$
-------	--

**4.6.13.1 Optically active constituents**

It is ~~set as a goal intended~~ to generate a ~~dataset~~SD that covers the widest possible range of optical water types. ~~As such, the~~ historic case 1 assumption is inappropriate, and an IOP definition based on a single index such as chlorophyll concentration (C) is therefore not adopted. Instead, a generic three-variables model is used, in which variability is driven by: ~~the chlorophyll concentration (C), the NAP concentration (N), and CDOM absorption at 440 nm (Y) C, N and Y separately.~~ However, ~~if~~ C, N and Y ~~shall not be~~ ~~were~~ completely independent ~~because, if that were the case,~~ the bio-optical modelling would generate unrealistic IOP combinations. Instead, ~~C, N and Y for a hypothetical large dataset that contains such variables, they are~~ ~~may be~~ expected ~~that they to~~ have a certain degree of general relationship, tighter for the smaller values, that are found in the ocean, ~~and more scattered for the higher values.~~

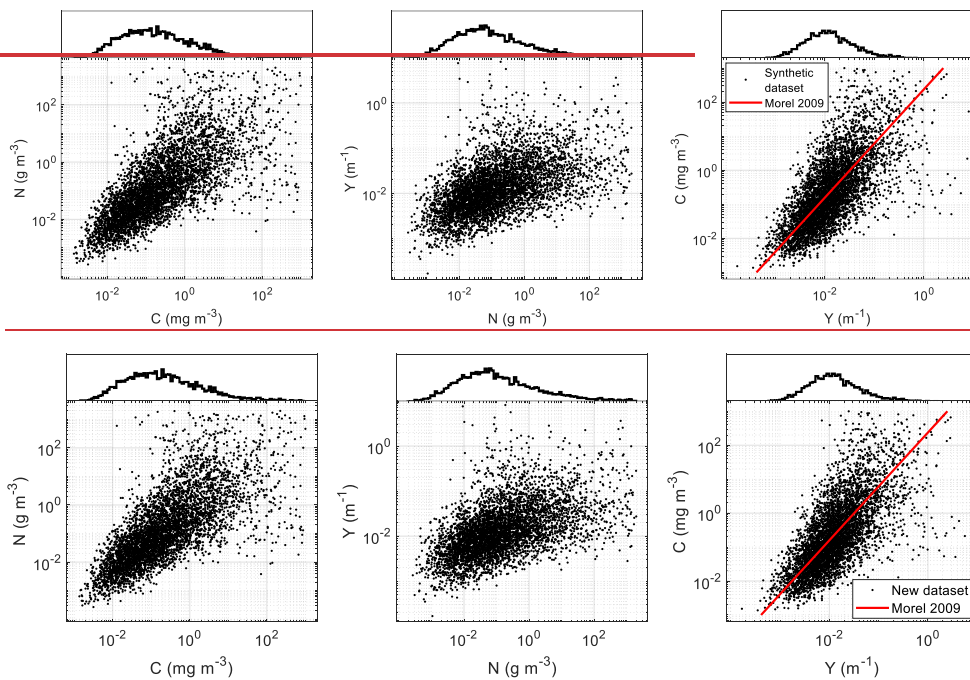
Here, the partial relationship between the three variables in logarithmic scale was modelled with the generation of 5000 triplets, following three Burr type XII random probability density functions,  $x \leftarrow \text{Burr}(\alpha, c, k)$ , related by a cross correlation matrix among them with the off-diagonal elements  $\rho_{CN} = 0.8$ ,  $\rho_{CY} = 0.75$ ,  $\rho_{YN} = 0.6$ . Then, the derived random numbers were transformed to the actual (C,N,Y), variables with  $X = 10^{x-d}$ , where X is either C, N or Y, and x is their logarithmic counterparts. ~~This is~~ ~~these~~ ~~parameters are~~ summarized in Table 2. ~~Finally~~ ~~Because the Burr distribution does not have an upper bound, it generated~~ very few outliers  $C > 1000 \text{ mg m}^{-3}$ ,  $N > 2000 \text{ g m}^{-3}$  and  $Y > 100 \text{ m}^{-1}$  (~0.2 % or less) ~~that~~ were considered excessive. ~~Such realizations~~ ~~and~~ were re-generated with a log-normal distribution, with the mean and standard deviation calculated from the rest of the dataset.

**Table 2 Parameters of the probabilistic modelling of the optically active constituents**

	Burr distribution parameters	Scale coefficient
--	------------------------------	-------------------

Formatted: Heading 2

Variable	$\alpha$	c	$k_k$	d
Chlorophyll concentration (C)	3	3	2	3
Non-algal particles concentration (N)	3	4	1	4
CDOM absorption coefficient at 440 nm (Y)	2	6	1.3	4



525 **Figure 1: Upper panels: histograms of the water constituents chlorophyll concentration (C), non-algal particles concentration (N) and CDOM absorption at 440 nm (Y). Lower panels: relationships between among them. For the relationship between C and Y, the relationship-average regression curve by Morel (2009) in oceanic waters is added for comparison.**

In Fig. 1, the outcomes of OAC generation are depicted, showcasing a broad spectrum ranges. The intentionally skewed data distributions were formulated skewed, to mirroring histograms observed in a broad range comprehensive global datasets: frequencies of data surge from the lower values, peak at

levels commonly encountered in global oceans, and gradually taper off at higher extremes. [Some degree of Concerning Regarding](#) interrelationships, [there](#) is observable ~~correlation~~, [which, in the case of C and Y, shows general agreement](#) with the empirical case 1 curve ~~identified~~ by Morel (2009) ~~—serving as a typical benchmark~~. ~~However, a~~As values ascend, the connection diminishes, consistent with expectations for coastal waters.

#### 1.6.23.2 Phytoplankton absorption and scattering

Phytoplankton absorption  $a_{ph}$  was modelled using data from the pool described in section ~~2.12.12.1.1~~. In order to generate phytoplankton diversity, it was important [to ensure](#) that, each time, a real  $a_{ph}$  spectrum was used. A similar approach to the  $a_{ph}$  generation in the IOCCG ~~dataset~~SD was followed, but first, it was found appropriate to revisit the relationship between C and  $a_{ph}$ . Matched data (Valente et al., 2022; Castagna et al., 2022) at several wavelengths (Fig. 2) revealed a tight linear relationship in log-log scale, though with some scatter, a part of which is attributable due to pigment variation. [Following Bricaud et al. \(1995\), a](#) power-law model [\(eq. \(8\)\)](#) was regressed at each wavelength:

$$a_{ph}(\lambda) \approx A(\lambda)C^{E(\lambda)} \quad (887)$$

**Table 3** Output variables [and statistical metrics](#) of the regression between matched chlorophyll concentration and phytoplankton absorption of the merged datasets Valente et al. (2022) and Castagna et al. (2022) at several bands.

$\lambda$ (nm)	411	443	489	510	555	670
A	0.043934	0.051348	0.03299	0.02132	0.0077002	0.019093
E	0.80289	0.77654	0.76732	0.8214	0.92914	0.95568
n	3509	3526	3525	3507	3231	2875
RMSE (%)	58.951	59.249	57.358	52.626	56.781	47.256
$r^2$	0.85688	0.84553	0.84846	0.88033	0.89645	0.92553

Table 3 presents the regression outcomes, including the two model parameters (A,E), data number (n), the root mean square in percent units and the coefficient of determination ( $r^2$ ). A comparison to results from previous publications (Churilova et al., 2023; Bricaud et al., 1995; Zibordi and Berthon, 2024) is

Formatted: Heading 2



made in Fig. 3, showing some discrepancies respect to the first three references but a high agreement with recent results by Zibordi and Berthon (2024).

555 Our results show that the 670 nm band has the highest capability for predicting C given  $a_{ph}$ . It is important to emphasize that ~~this calculation~~ our modelling does not ~~model-generate~~  $a_{ph}$  for a specific C; rather, it associates each  $a_{ph}$  with its characteristic "C", from inversion of eq. (87). This ~~facilitates-enables to the~~ sorting of the 3025  $a_{ph}$  spectra based on "C", dividing them into 55 pools of specific "C" sub-ranges, each containing 55 spectra. Consequently, for a given C value from the (C,N,Y) triplet, a random  $a_{ph}$  spectrum from the corresponding pool is selected. Subsequently, the spectrum is adjusted by a factor so that  $a_{ph}(670)$  equals the predicted  $a_{ph}(670)$  from C, after eq. (887). This methodology guarantees consistency between  $a_{ph}$  and empirical evidence for a given C while ensuring a broad diversity in  $a_{ph}$  spectral shapes.

560

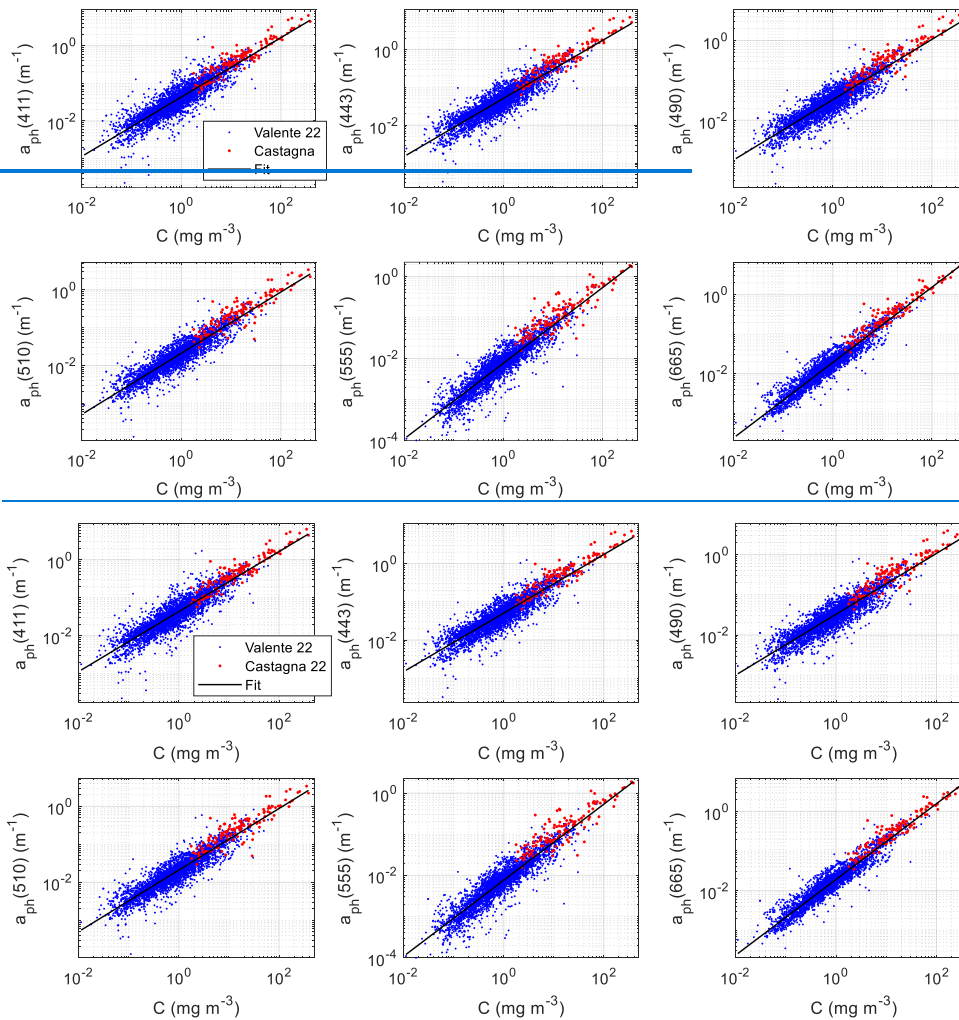
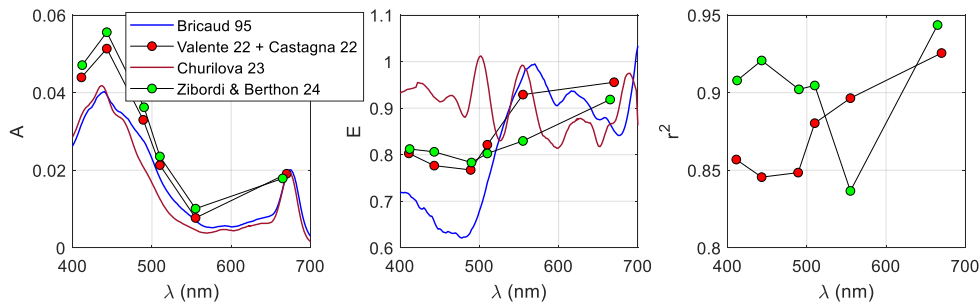
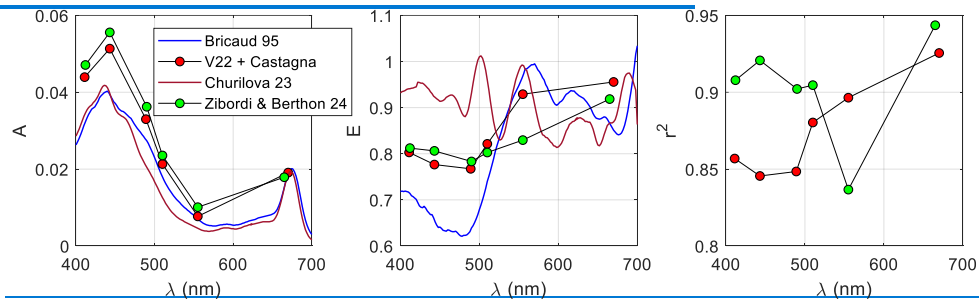
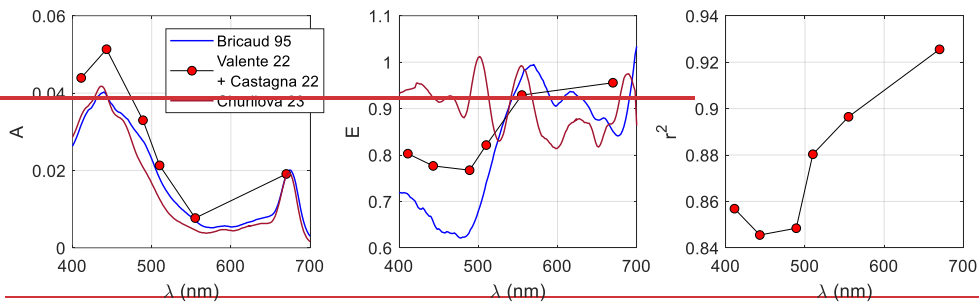


Figure 2: Matched  $C$  and  $a_{ph}$  data (Valente et al., 2022; Castagna et al., 2022) at six wavelengths. A linear fit in log-log form is displayed on top.



**Figure 3: Regression statistics of the fit between C and  $a_{ph}$  data of Fig. 2. Left and center plots are Bricaud's A and E parameters, whereas the right plot is the coefficient of determination ( $r^2$ ).**

Phytoplankton scattering ( $b_{ph}$ ) modelling unfortunately has much less background knowledge, mostly due to the lack of instruments that can measure in situ  $b_{ph}$  or  $b_{b,ph}$ . ~~Still, there are some~~

~~notable~~ Electromagnetic modelling of light scattering by particles suspended in water can be applied, although the contributions, albeit notable, are limited modelling contributions based on electromagnetic theory (Lain et al., 2023; Poulin et al., 2018).

Upon this lack, it is often referred to historic measurements by Loisel and Morel (1998) of non-water beam attenuation coefficient at 660 nm  $c_{nw}(660)$  with a transmissometer, matched to chlorophyll concentration in case 1 waters. For ~~the surface layer waters,~~ they found  $c_{nw}(660) = 0.407C^{0.795}$ . Furthermore, the authors reasonably assumed that the dissolved contribution was secondary, so  $c_p(660) \approx c_{nw}(660)$ . Unfortunately, this relationship was directly exported to phytoplankton scattering modelling used in the ~~CoastColour~~ CoastColour datasetSD (Nechad et al., 2015), replacing  $c_p(660)$  with  $c_{ph}(660)$ , ignoring that even in open sea waters, the non-algal scattering is considerable.

~~(IOCCG, 2006; Loisel et al., 2023) Instead Here, a random coefficient was used for phytoplankton attenuation the same generic, while leaving the power law dependence as in the IOCCG SD the in the IOCCG dataset (IOCCG, 2006) is used, a random coefficient was used for phytoplankton attenuation, while leaving the power dependence:~~

$$c_{ph}(660) = p_3 C^h \quad (998)$$

According to the IOCCG report,  $h = 0.57$ , although application of eq. (998) to the downloadable datasetSD reveals  $h = 0.63$ . In the CoasColour datasetSD,  $h = 0.795$ . Here,  $h = 0.7$  is used as a balance of both.

~~On  $p_3$ , it~~ was set random between 0.06 and 0.6 in the IOCCG datasetSD. Interestingly, that leaves the contribution of phytoplankton mostly below what found by Loisel and Morel (1998) for the total attenuation, which appears physically meaningful. The type of randomness of  $p_3$  was not disclosed, but an inspection to the IOCCG datasetSD revealed that it was uniform. This parameter is is left unchanged for the modelling here like in the IOCCG datasetSD of the current dataset given the absence of empirical evidence that justifies otherwise.

The spectral variation is set by assigning a power law to ~~phytoplankton attenuation  $c_{ph}$ .~~ This choice, i.e. In fact, modelling the spectral variation of attenuation rather than of scattering, with a simple and featureless function, has physical justification. A power law function provides a better fit for

$c_{ph}$  attenuation than for  $b_{ph}$  scattering, as the latter is affected by anomalous dispersion effects, that result in some negative peaks with the shape of an  $a_{ph}$  absorption spectrum, more evident at high phytoplankton concentrations (Bernard et al., 2009). Interestingly, if the power law function is imposed to  $c_{ph}$ , the anomalous dispersion features  $b_{ph}$  automatically appear after  $b_{ph} = c_{ph} - a_{ph}$ . Therefore, in the current SD, neither  $b_{ph}$  nor  $b_{b,ph}$  follow power law functions.

Regarding the actual exponent of the spectral power law in the absence of further information, the same relationship as in the IOCCG dataset SD is used, that is (eq. (10)):

$$c_{ph}(\lambda) = c_{ph}(660) \left( \frac{660}{\lambda} \right)^{n_1}, \text{ with } n_1 = -0.4 + \frac{1.6+1.2\mathfrak{R}}{1+C^{0.5}} \quad (10)$$

With  $\mathfrak{R}$  being a random number that follows a uniform distribution in the interval [0,1].

Given the randomness of  $a_{ph}$  and  $c_{ph}$ , it is possible that some realizations generate cases where  $a_{ph} \geq c_{ph}$ , which is unphysical. Indeed, a given  $a_{ph}$  represents an certain community-assemblage of several phytoplankton communities, which have each with their specific scattering characteristics, that could be somewhat predicted given  $a_{ph}$ . Unfortunately, there is a lack of knowledge on how to parameterize  $c_{ph}$  or  $b_{ph}$  scattering when  $a_{ph}$  absorption is known. This information could be extracted from the fine spectral features of  $a_{ph}$ .

There are some simplified modelling results using electromagnetic theory for certain phytoplankton species (Lain et al., 2023), although a general modelling theory of phytoplankton scattering linked to absorption is still non-existent. Thus, in this dataset SD, as in the precedent ones (IOCCG, 2006; Nechad et al., 2015; Loisel and Morel, 1998),  $a_{ph}$  and  $c_{ph}$  are modelled independently, yet related to the same chlorophyll concentration. To ensure a minimum degree of physical consistency, a condition was set, that if there were any bands at which  $a_{ph} \leq c_{ph}$ , the procedure for determining  $a_{ph}$  and  $c_{ph}$  should be repeated until ensuring  $a_{ph} < c_{ph}$  at all wavelengths.

The remaining parameter that must be set to run Hydrolight is the phytoplankton backscattering ratio,  $B_{ph} = \frac{b_{b,ph}}{b_{ph}}$ . This parameter has not been given much importance-attention in previous research, as it was considered relatively unimportant, so it is common to find it set to a constant value in the order of 0.006 or 0.01. It is indeed secondary in semi-analytical models-algorithms that model  $R_{rs}$  from  $\frac{b_b}{a+b_b}$  or

630 variations, but in bio-optical modelling it can be very relevant if  $b_{ph}$  is fixed first, because then,  $b_{b,ph}$  is implicitly determined through the choice of the respective phase function given  $B_{ph}$  (Mobley et al., 2002), thereby ~~setting the~~ strongly influencing the intensity of  $R_{rs}$  the signal. ~~Fixing  $b_{b,ph}$  first as a function of C would be another modelling option, for instance by adapting relationships between  $b_{bp}$  and C found in the ocean (Brewin et al., 2012) to  $b_{b,ph}$ .~~

~~In an attempt effort to provide a more accurate We pursued a determination of  $B_{ph}$  than in previous approaches, that we propose a formula that is was consistent with the general trend that phytoplankton size increases with C. This In its turn, size increase has a diminishing effect on lowers  $B_{ph}$  because larger larger  $B_{ph}$  is associated with smaller particles, which scatter relatively more in the backward-forward hemisphere respect to larger-smaller ones, hence lowering  $B_{ph}$ . Also, smaller particles have a larger surface area per unit volume, which enhances scattering. A single variable mechanistic model for  $b_{bp}$  that agrees with this principle was presented in Brewin et al. (2012). In terms of the backscattering ratio,~~

640 Twardowski et al. (2001; Fig. 11) presented pioneering results, for  $B_p$  in their case. Here, to mimic such effect, ~~we it is~~ set

$$B_{ph} \sim \mathcal{N}(\mu, \sigma)$$

$$\mu = 0.002 + (0.01 - 0.002) \exp[-0.56 \log_{10}(C)], \sigma = 0.001(3 - \log_{10}(C)) + 0.001 \quad (111110)$$

To avoid unlikely low  $B_{ph}$  values after eq. (111110), any realization delivering  $B_{ph} < 0.001$  was set to

645 0.001 as a lower limit.

**Commented [JP4]:** Added to provide some alternatives to the modelling choices, as requested by reviewer McKee

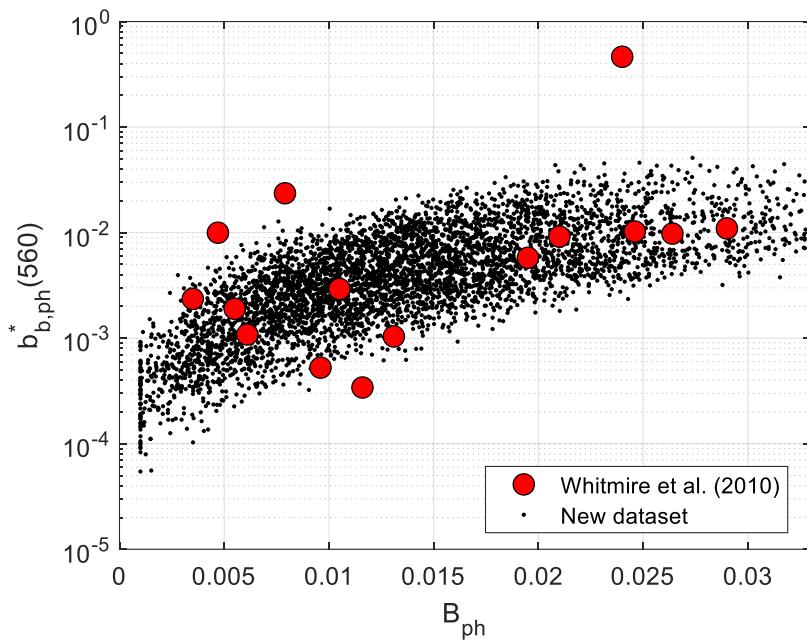


Figure 4: Phytoplankton backscattering ratio  $B_{ph}$  vs. phytoplankton specific backscattering coefficient at 560 nm  $b_{b,ph}^*(560)$ . Black dots: [new synthetic datasetSD](#). Red dots: data in Whitmire et al. (2010)

650 ~~Independent validation of The the~~ modelling of phytoplankton scattering ~~we just presented in eq. (11) has~~  
~~some is~~ possible ~~unique with data of chlorophyll concentration matched to scattering and backscattering~~  
~~for an array of phytoplankton cultures independent validation by~~ Whitmire et al. (2010) ~~presented unique~~  
~~data of chlorophyll concentration matched to scattering and backscattering for an array of phytoplankton~~  
~~cultures. Their data of Calculating~~ the chlorophyll-specific phytoplankton backscattering coefficient, i.e.,

655  $b_{b,ph}^* = \frac{b_{b,ph}}{c}$  at 560 nm, ~~and matching it to matched to~~  $B_{ph}$  produces dot clouds in Fig. 4. Our new  
~~synthetic datasetSD follows the average trend displayed by the Whitmire et al. (2010) in situ data are~~  
~~fairly well on top of the data cloud of this synthetic dataset (Fig. 4), also verifying the positive correlation~~  
~~of the two variables to a first order. Fig. 4 also shows some degree of positive covariation~~  
~~between According to scattering theory,  $b_{b,ph}^*$  and  $B_{ph}$ . Indeed,  $b_{b,ph}^*$  should also increase/decrease with~~

660 ~~decreasing~~increasing  $C$  as well, as because ~~smaller~~larger particles have a ~~larger~~smaller surface area per unit volume, which ~~enhances~~diminishes specific scattering. A mechanistic model for  $b_{bp}$  that agrees with this principle was presented in Brewin et al. (2012). All in all, this leads to the visible correlation between  $B_{ph}$  and  $b_{b,ph}^*$  with the scatter caused by species differences.

### 1.6.3.3 NAP absorption and scattering

665 Bio-optical modelling of NAP absorption  $a_{NAP}$  is complex, as NAP is formed by particles of very diverse nature, of biogenic and non-biogenic origin. Modelling approaches (Bengil et al., 2016) are valid as long as the derived relationships hold for the specific area of application. Here, it is aimed at a modelling approach of general validity, consistent with the in situ datasets that were collected from worldwide waters.

670 Modelling ~~starts~~begins with ~~requires~~ linking  $a_{NAP}$  to the ~~mass~~-NAP concentration,  $N$ , through the specific absorption (to NAP concentration)  $a_{NAP}^*$ . Taking 440 nm as the reference band, other approaches have set it to a constant value (Nechad et al., 2015), ~~but~~although a variability between 0.001 and 0.1 m<sup>2</sup> g<sup>-1</sup> was reported by Results in Blondeau-Patissier et al. (2009) suggested that  $a_{NAP}^*(440)$  varies between 0.001 and 0.1 m<sup>2</sup> g<sup>-1</sup>. When looking for a predictive formula, ~~One~~one may ~~assume~~think that ~~such~~the

675 ~~actual~~ value depends on the type of particles. Following this consideration, ~~here~~, the ratio  $C/N$  is proposed ~~here~~ as a first-order predictor of  $a_{NAP}^*(440)$ . This dependence assumes that ~~non-algal particles~~NAP absorbs more efficiently in the relatively higher presence of chlorophyll, which suggests that ~~they~~NAP may be of biogenic origin to a larger extent than if the chlorophyll concentration was relatively lower, where ~~they~~NAP may be more of a mineral origin instead. CSIRO data confirmed some degree of covariation (Fig. 5). The fit to the CSIRO data was made in logarithmic scale, so  $y = \log_{10}[a_{NAP}^*(440)]$  was regressed as a function of  $x = \log_{10}\left(\frac{C}{N}\right)$ , proposing a functional form of the type  $y = a \exp(bx) + c$ . A robust regression (bi-square weighting) gave  $a = -0.1886, b = -1.0551, c = -1.2700$ . The standard deviation of the fit was  $\sigma = 0.2627$ . To generate the synthetic data, given  $C/N$ , the regression curve was applied and then a random value, generated with a normal distribution  $\mathcal{N}(0, \sigma)$  was added,

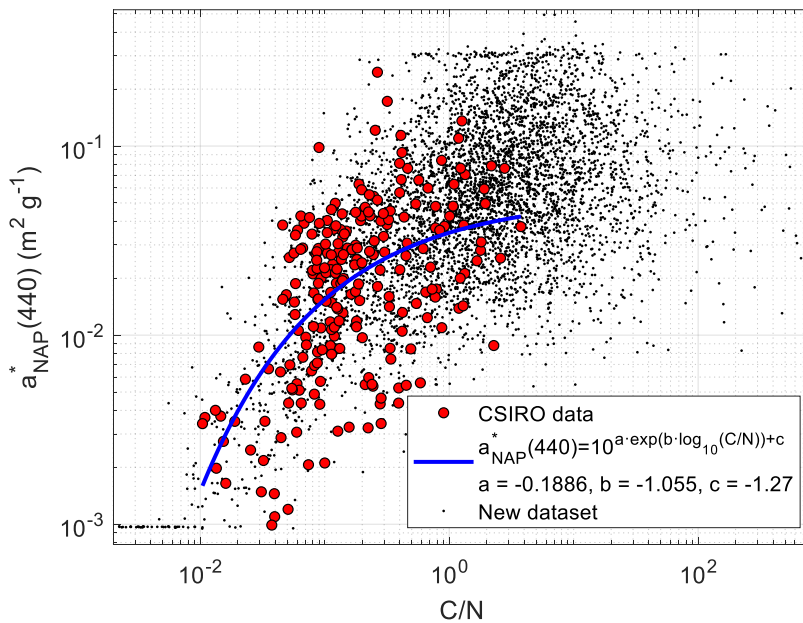
685 in order to replicate the spread found in real data.  $\frac{C}{N}$  in our ~~synthetic dataset~~SD covers a wider range than

Formatted: Heading 2

Commented [JP5]: Addition after request by reviewer McKee



CSIRO's data, so, to avoid producing resulting synthetic  $a_{NAP}^*(440)$  values much out of the range of the measured data, the lower and upper bounds of -3 and -0.5 were set for  $\log_{10}[a_{NAP}^*(440)]$ . The results are shown in Fig. 5.



690 **Figure 5: Non-algal particles specific absorption coefficient at 440 nm  $a_{NAP}^*(440)$ , plotted as a function of the chlorophyll to NAP concentrations ratio  $C/N$ . Results for CSIRO data in red dots, a best fit in blue, and generated data for the [synthetic datasetSD](#) (black dots).**

Posteriorly, it is necessary to project  $a_{NAP}^*(440)$  to all bands. It can be done by assuming an exponential spectral shape and then guessing a spectral slope ( $S_{NAP}$ ). Historic data [suggested an average showed a](#)  
 695 [distribution of  \$S\_{NAP}\$  with an average](#) value of 0.0123  $\text{nm}^{-1}$  (Babin et al., 2003), though with a [visible significant](#) spread. Using a single average  $S_{NAP}$  for all simulations removes optical diversity and likely generates  $a_{NAP}^*$  spectra that are unlikely for some regions. It is a better choice to generate a prediction function for  $S_{NAP}$  given the available information. After the exponential fits for each of the compiled

$a_{NAP}$  spectra, detailed in section 2.32.1.3, the 1349  $(a_{NAP}(\lambda_0), S_{NAP})$  pairs  $a_{NAP}(440)$  and  $S_{NAP}$  were calculated and plotted together in Fig. 6.

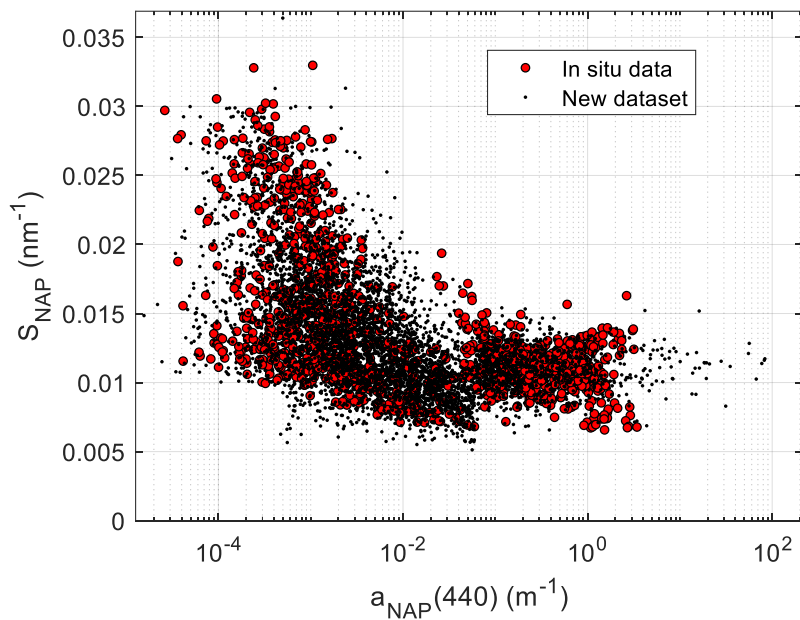


**Figure 6: Non-algal particles absorption spectral slope ( $S_{NAP}$ ), plotted as a function of the NAP absorption coefficient at 440 nm ( $a_{NAP}(440)$ ). Red dots: in situ data. Black dots: synthetic data.**

The data distribution in Fig. 6 shows a  $S_{NAP}$  spread that largely varies depending on the  $a_{NAP}$  range. For very small  $a_{NAP}$  values,  $S_{NAP}$  data shows no particular pattern between two bounds, so a uniform distribution was found adequate. For the middle range, the  $S_{NAP}$  distribution somewhat narrows as  $a_{NAP}(440)$  increases, and data shows some positive skewness, which is well represented by a log-normal curve. For the higher  $a_{NAP}(440)$  range, a gaussian distribution was observed apparent, in agreement with Babin et al. (2003). Therefore, given  $x = \log_{10}[a_{NAP}(440)]$ ,  $S_{NAP}$  was modelled as a piece-wise

random distribution:

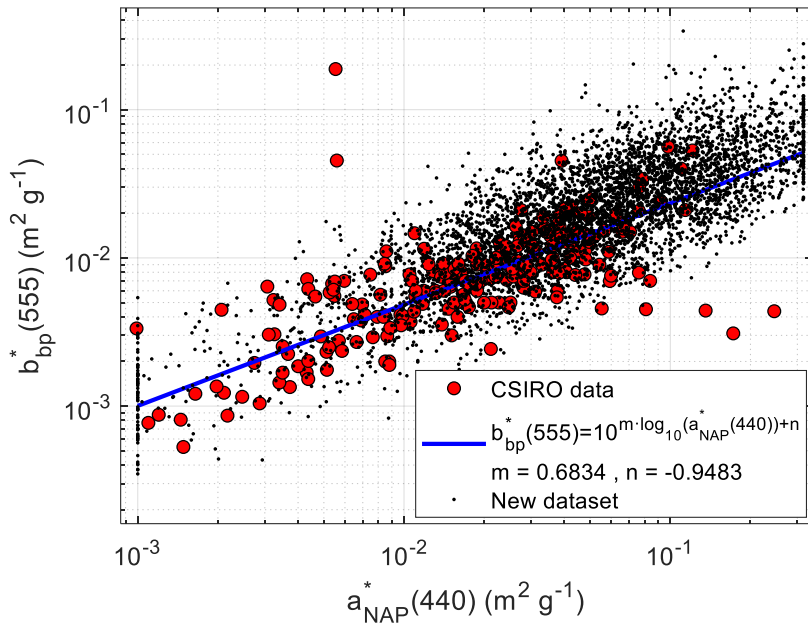
$S_{NAP} \leftarrow$

$$\begin{cases} \mathcal{U}\mathcal{U}(0.01, 0.035) & \text{if } a_{NAP}(440) < 4 \cdot 10^{-4} \text{ m}^{-1} \\ \text{Ln } \mathcal{N}\mathcal{N}(-0.308x - 5.101, -0.0558x + 0.1164) & \text{if } a_{NAP}(440) \in [4 \cdot 10^{-4}, 0.06] \text{ m}^{-1} \text{ (121211)} \\ \mathcal{N}\mathcal{N}(0.011, 0.016) & \text{if } a_{NAP}(440) \geq 0.06 \text{ m}^{-1} \end{cases}$$

Where  $\mathcal{U}\mathcal{U}(a, b)$ ,  $\text{Ln } \mathcal{N}\mathcal{N}(\mu, \sigma)$  and  $\mathcal{N}\mathcal{N}(\mu, \sigma)$  are the uniform, log-normal and normal distributions, respectively. The random parameterization for  $S_{NAP}$  in eq. (121211) is rather convoluted. However, it ensures fitness to a high quality and large in situ dataset ~~present in Fig. 6,~~ and it does not generate outliers, ~~as it can be seen when overlapping the synthetic data to the field data in Fig. 6.~~

NAP scattering needs bio-optical modelling too. Approaches that model NAP absorption and scattering independently may generate unrealistic IOPs for that particular material. It is beneficial to look for relationships that link NAP scattering to NAP absorption, as it is expected to occur in ~~reality~~natural waters.

The CSIRO dataset ~~provides~~contains  $b_{bp}^*$ (555) data, concurrent to  $a_{NAP}^*(440)$ . It must be clarified that, ~~while~~  $a_{NAP}^*(440)$  is specific of N,  $b_{bp}^*$  has been defined by normalizing  $b_{bp}$  to the total suspended matter concentration (T), not to be confused with non-algal particles concentration N, as the latter is only a fraction of the former, which also contains the phytoplanktonic part. Brando and Dekker (2003) proposed a somewhat crude relationship,  $T = N + 0.07C$ , where both T and N are expressed in the usual units of  $\text{g m}^{-3}$  and C is in  $\text{mg m}^{-3}$ . For interested readers, such relationship was derived from measurements ~~at-in~~ a shallow, turbid and eutrophic lake in The Netherlands (Gons et al., 1992).



730 **Figure 7: Specific particle backscattering coefficient at 555 nm  $b_{bp}^*(555)$ , plotted as a function of the non-algal particles specific absorption coefficient at 440 nm  $a_{NAP}^*(440)$ . Results for CSIRO data in red dots, [the best linear fit in blue](#), and generated data for the [synthetic datasetSD](#) (black dots).**

The relationship between  $a_{NAP}^*(440)$  and  $b_{bp}^*(555)$  data [appeared to be is](#) very [significant-marked](#) (Fig. 7, red dots). A linear trend was a very good fit between the log-transformed variables, with a slope  $m = 0.6834$  and an intercept  $n = -0.9483$ . The data spread followed a normal distribution ( $\sigma = 0.2627$ ) after removing the trend line. To reproduce this spread in the [synthetic datasetSD](#), a random number following a random normal distribution  $N(0, \sigma)$  was added to the fit-predicted  $b_{bp}^*(555)$ , prior to conversion to linear scale again. Results of the [generated](#) data cloud [generated](#) are seen in Fig. 7, black dots.

740 Completing the bio-optical modelling for NAP requires [that to project  \$b\_{bp}^\*\$  is given at 440 nm, which implies projecting  \$b\_{bp}^\*\$  from 555 nm with some sort of spectral parameter](#). CSIRO data provides

an estimate of the particle backscattering spectral slope ( $\eta$ ) for every data point. For the synthetic data generation, a modelling function for  $\eta$  must be derived. No relationship between  $\eta$  and any other parameter within the CSIRO dataset was found, so instead of simply setting  $\eta$  to an average value, its histogram was fitted well to with a random Burr distribution with the parameters  $\alpha = 0.854, c = 4.586, k = 1.108$ , shown in Fig. 8. Therefore,  $\eta$  was randomly generated using this distribution.

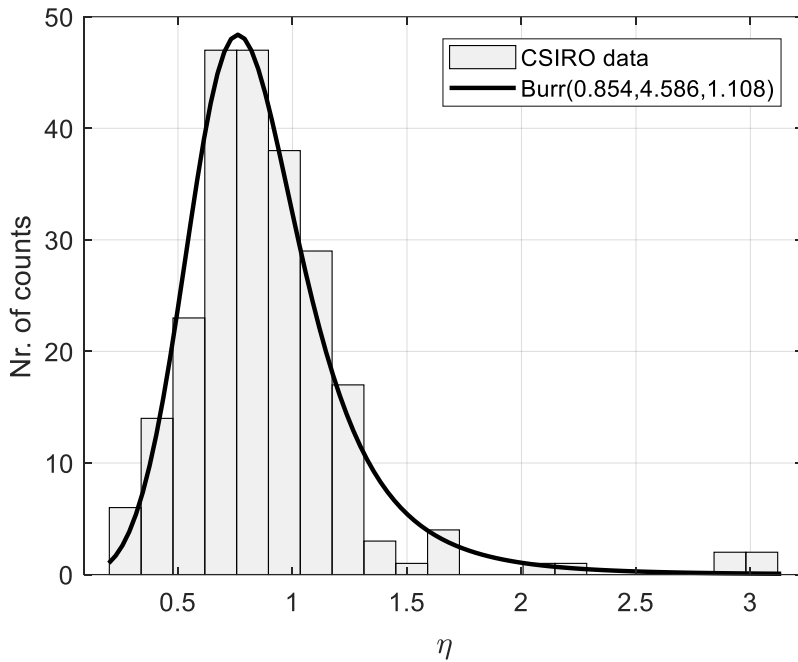


Figure 8: Histogram of the particle backscattering coefficient spectral slope ( $\eta$ ). A Burr Type XII fitted distribution is plotted on top.

Therefore, after randomly generating the slope  $\eta$  determined,  $b_{bp}^*$  was randomly generated with such distribution,  $b_{bp}^*$  is was shifted to 440 nm: so that  $b_{bp}^*(440) = b_{bp}^*(555) \left(\frac{440}{555}\right)^{-\eta}$ . It must be noted remarked that this  $b_{bp}$  slope is only used in this step and it is not used to model  $b_{bp}$  with a power law in

Formatted: Font: Cambria Math, Italic

Formatted: Font: Cambria Math, Italic

Formatted: Font: Cambria Math, Italic

~~the SD propagate backscattering or any other IOP to the full spectral range.~~ In the bio-optical modelling of NAP, ~~as well as~~ and of phytoplankton, a spectral shape is assumed for attenuation, not for backscattering.

The NAP backscattering at 440 nm ~~is was~~ derived in eq. (13) by subtraction of the phytoplanktonic part, which is known from section 3.23.22.2.2:

$$b_{b,NAP}(440) = b_{bp}^*(440) \cdot T - b_{b,ph}(440) \quad (131312)$$

A backscattering ratio for NAP ( $B_{NAP}$ ) must be assumed to obtain  $b_{NAP}(440)$  and  $c_{NAP}(440)$ . There are no direct measurements of  $B_{NAP}$  given the current impossibility of measuring NAP scattering parameters in the field. Nevertheless, this poses a minor problem for radiative transfer calculations, especially for remote sensing applications. As long as  $b_{b,NAP}$  is fixed,  $B_{NAP}$  is relatively unimportant, as one can deduct from simplified analytical models for reflectance or diffuse attenuation. If  $b_{NAP}$  were fixed instead,  $B_{NAP}$  would be a fundamental parameter, as it would implicitly set  $b_{b,NAP}$ , in a much less accurate fashion.

$B_{NAP}$  ~~is was~~ here fixed as a random number, following a uniform distribution between 0.01 and 0.02 as in eq. (1514):

$$B_{NAP} \leftarrow \mathcal{U}(0.01, 0.02) \quad (141413)$$

~~Therefore,~~ the scattering coefficient of NAP was determined with eq. (15):

$$b_{NAP}(440) = \frac{b_{b,NAP}(440)}{B_{NAP}} \quad (151514)$$

Then, the NAP attenuation at 440 nm ~~was~~ expressed in eq. (16) as a function of values that are all known:

$$c_{NAP}(440) = a_{NAP}^*(440) \cdot N + b_{NAP}(440) \quad (161615)$$

The remaining step for NAP modelling is extending NAP attenuation ~~is extended~~ to all wavelengths. As for phytoplankton, a ~~as a~~ power law. As for phytoplankton, is assumed, and it is preferred to impose it ~~fit a power law~~ to attenuation than to scattering, though recognizing that, given the much featureless shapes of NAP absorption, a fit to scattering may be realistic too. A  $c_{NAP}$  spectral slope  $\gamma_{NAP}$  must be ~~derived~~ assumed. This parameter is largely unknown as it cannot be measured in the field. Here, an educated guess is made, generating  $\gamma_{NAP}$  randomly, with  $\gamma_{NAP} \leftarrow \mathcal{N}(0.7, 0.3)$ . Therefore, eq. (17) completes the NAP modelling:

780  $c_{NAP}(\lambda) = c_{NAP}(440) \left(\frac{440}{\lambda}\right)^{Y_{NAP}}$  (17)

**1.6.43.4 CDOM absorption**

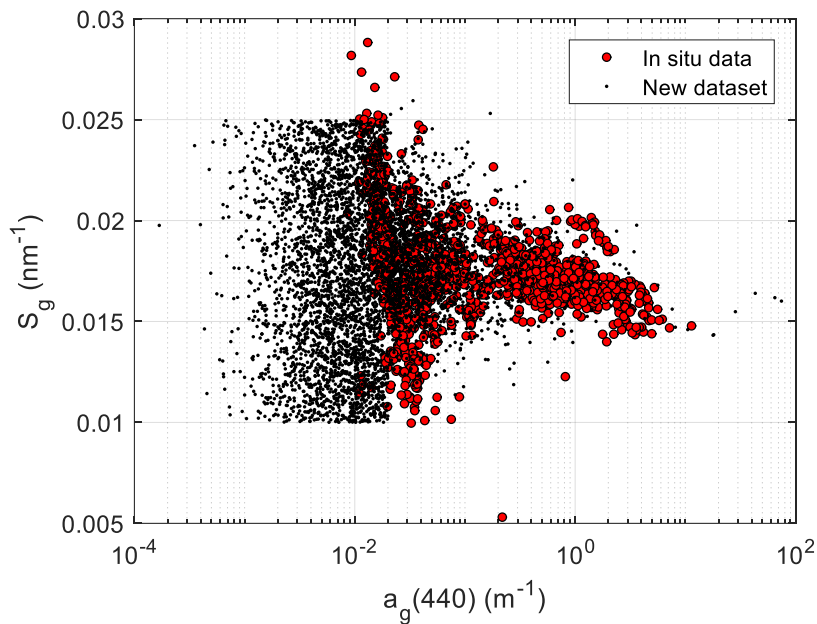
The 1168  $(a_g(\lambda_0), S_g)$  pairs ~~The same procedure as for the NAP absorption coefficient is followed here, as detailed in section 2.22.1.2: exponential functions were fitted to the  $a_g$  spectra, and from those regressions having very high correlation,  $a_g(440)$  and  $S_g$  were retained~~ are plotted together in Fig. 999. The middle section shows a data spread, whose mean and standard deviation decrease with  $a_g(440)$ . Variation in the lower and upper range ends could not be linked to any parameter, so that  $S_g$  was modelled as uniform distributions, fairly within the data range. Overall,  $S_g$  was then modelled as a piece-wise random distribution ~~G~~ given  $x = \log_{10}[a_g(440)]$ :

790  $S_g \leftarrow$

$$\begin{cases} \mathcal{U}(0.01, 0.025) & \text{if } a_g(440) < 0.02 \text{ m}^{-1} \\ \mathcal{N}(-0.00040161x + 0.017508, -0.0003012x + 0.001881) & \text{if } a_g(440) \in [0.02, 5) \text{ m}^{-1} \\ \mathcal{U}(0.0143, 0.017) & \text{if } a_g(440) \geq 5 \text{ m}^{-1} \end{cases}$$

Formatted: Heading 2

Formatted: Font: Not Bold



795 **Figure 9: CDOM spectral slope ( $S_g$ ), plotted as a function of the CDOM absorption coefficient at 440 nm ( $a_g(440)$ ). Red dots: in situ data. Black dots: synthetic data.**

800 Fig. 99 compares the field ( $a_g(\lambda_0), S_g$ ) pairs to those generated with the combination of random distributions in eq. (1847). It is shown can be seen that the synthetic datasetSD includes many points an order of magnitude more of below the lower  $a_g(440)$  at the lower end than the in situ data in Fig. 99.

805 limit. This is due to the very stringent condition of exponential variation set in section 2.2, that mostly affected the low  $a_g$  spectra. This is a consequence of the well known under sampling of the oligotrophic oceans. In terms of predicting  $S_g$ , Extrapolation may raise some concerns, but on one hand,  $S_g$  values are well bounded in this part of the range, and on the other hand, one must also note that  $a_g(440)$  becomes very low, so that potential errors in  $S_g$  are not relevant for the absorption budget. In terms of data range, it will be shown in section 4.1 that the lowest  $a_g(440)$  in the datasetSD are in the order of  $a_g(440)$  in

Formatted: Font: Not Bold

Formatted: Font: Not Bold



~~the most oligotrophic oceans. This is a consequence of the well-known under-sampling of the oligotrophic oceans. Extrapolation may raise some concerns, but on one hand,  $S_{\text{ph}}$  values are well bounded in this part of the range, and on the other hand, one must also note that  $a_{\text{ph}}(440)$  becomes very low, so that potential errors in  $S_{\text{ph}}$  are not relevant for the absorption budget.~~

Commented [JP6]: In response to reviewer McKee

#### 1.6.5.3.5 Pure water absorption and scattering

Formatted: Heading 2

Pure liquid water absorbs electromagnetic radiation, which can be ~~intuitively-mechanistically~~ explained as the energy ~~being used~~ consumption by the two O-H molecular bonds to vibrate at given resonant frequencies, creating an absorption spectrum  $a_w$  with characteristic maxima and minima at specific wavelengths. ~~In practice,  $a_w$  must be measured at a wide enough spectral range and its values be tabulated for usage in bio-optical modelling.~~

~~However, Literature literature only offers partial spectral range  $a_w$  measurements for pure water absorption, owing to the specific requirements and challenges inherent in such measurements across different spectral regions. Factors such as signal to noise ratio, sample purity, and instrument cleanliness contribute to this variability. A broad range  $a_w$  must then be a merged product from individual sources.~~

~~When compiling a comprehensive dataset spanning a broad range, a crucial step here involves normalization to a common temperature compensating for the different temperatures at which  $a_w$  was measured in different laboratories and, in the spectral ranges where different measurements are available, selecting those that are retained of the highest quality.~~ Fortunately, this ~~merging~~ process was already

undertaken within the framework of an ESA project (Roettgers et al., 2016), where the "water optical properties processor" (WOPP) produced a ~~consolidated~~ dataset of pure water absorption, normalized to 20°C. Notably, this dataset encompasses measurements by Mason et al. (2016) from UV to green wavelengths, revealing lower water absorption in the UV and blue regions than previously documented, thanks to meticulous sample preparation and precise measurements. In other spectral regions, data from various authors are merged, sometimes overlapping spectrally and sometimes not. Overall, the WOPP pure water absorption data can be considered the state of the art. For comprehensive insights, readers are directed to the project report.

When marine salts are dissolved in water, the ions ~~are dissociated~~ and create a stable solution whose absorption can be related to that of pure water proportionally to the ~~concentration of salt for the range of salinities ( $\Psi_S$ ) that is commonly encountered, although this proportionality coefficient is~~ wavelength dependent. Temperature affects absorption in a similar manner through  $\Psi_T$ , thus leading to:

$$a_w(T, S) = a_w(T_0, 0) + \Psi_T(T - T_0) + \Psi_S S \text{ (194817)}$$

Both  $\Psi_T$  and  $\Psi_S$  can be empirically determined. To the WOPP pure water merged absorption, a shift to an average ocean salinity of S=35 PSU was made with eq. (194817), using the  $\Psi_S$  coefficient provided by Roettgers et al. (2014) for artificial seawater.

Scattering by pure water finds explanation with the Smoluchowski-Einstein fluctuation theory of light scattering (Zhang and Hu, 2021), according to which, a certain volume of water can be seen as made of smaller sub-volumes that contain, on average, the same number of water molecules. However, the instantaneous numbers vary among them due to random thermal motions at the molecular level, resulting in microscopic density fluctuations that induce scattering. In the presence of solutes such as salts, this effect is magnified, as fluctuations in the spatial arrangement of dissolved ions lead to variations in the overall refractive index. For common ocean salinities, scattering is augmented by approximately 30% respect to fresh water. Recent work by Zhang and Hu (2021) provides a comprehensive review of this theory, offering the most precise estimates to date (likely within  $\pm 2-4\%$ ). Nevertheless, rigorous experimental validation remains imperative. The formulas provided as supplementary material in their paper were employed to compute seawater scattering, assuming a temperature of T=20°C and a salinity of S=35 PSU, as for the absorption data.

## **2.4. Results of the synthetic dataset**

### **2.4.1 Modelled IOPs**

The bio-optical modelling detailed in the section ~~3.2.2~~ generated the IOPs that determine the resulting light field and related AOPs, given the boundary conditions. These bio-optical relationships have been individually assessed and consistency with literature and with new data has been ensured in that section. However, the overall result of the bio-optical modelling can be tested~~a further test is desirable~~possible.

~~that implies~~by checking the crossed relationship between different commonly measured IOPs at specific wavelengths, compared to ~~all available~~ in situ data, in order to verify that the relationships that are found  
860 in the world's waters are represented.

~~In situ D~~datasets were searched that contained IOP data at the reference wavelength of 440 nm. The following publicly available ~~in situ~~ data were used: PACE data including the BIOSOPE-Biosope cruise data from the clearest ultraoligotrophic waters of the south-Pacific gyre, plus some stations in coastal upwelling water off Perú, and Mouw's data in Lake Superior (Casey et al., 2020), the NOMAD dataset  
865 (Werdell and Bailey, 2005), Castagna's data in Belgian coastal and inland waters (Castagna et al., 2022), measurements in coastal European waters (Massicotte et al., 2023), ~~Mouw's data in Lake Superior (Casey et al., 2020), and recent~~ measurements in Svalbard-Svalbard (Petit et al., 2022) and a recently published dataset in European seas (Zibordi and Berthon, 2024). In addition, two datasets not yet publicly available were queried to the authors, who kindly sent them for use in this article: data from the Persian Gulf  
870 (Moradi and Arabi, 2023) and from Australian waters (Blondeau-Patissier et al., 2009; Blondeau-Patissier et al., 2017; Cherukuru et al., 2016; Oubelkheir et al., 2023; Brando et al., 2012). ~~In this latter case Castagna's data lacked;  $b_{bp}$  was not available, but since such a dataset are~~is was considering especially important for their very high values unique and relevant,  ~~$b_{bp}$  was~~ inferred through semi-analytic closure from absorption and  $R_{rs}$  (Lee et al., 2011).

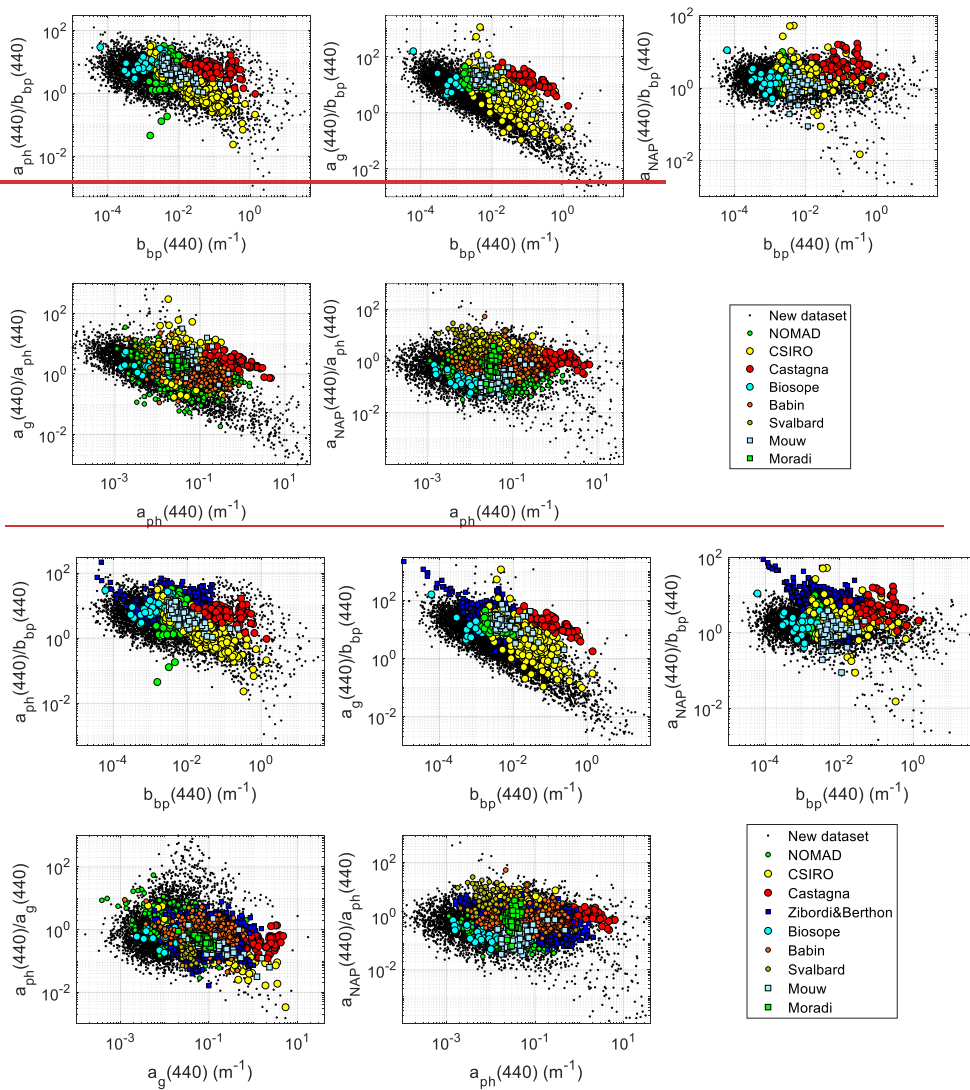


Figure 10: IOP cross-relationship comparison between the [synthetic dataset SD](#) and various in situ datasets.

Fig. 10 presents relationships among various IOPs at the reference ~~wavelength~~wavelength of 440 nm. The upper panels study the three non-water absorption components with respect to particle backscattering and the two lower panels ~~study compare the different absorption compartments~~the CDOM and NAP absorption with respect to phytoplankton absorption. ~~Given that any pair of~~Because two given IOPs are expected to linearly covary to the first degree, the vertical axis plots the ratio between the two, so that the linear covariation is eliminated, restricting the dynamic range and highlighting the differences among datasets. The plots show that available measurements in different ~~regions~~geographic areas and seasons cover different regions of the data space, and that the ~~synthetic dataset~~SD ~~nicely globally~~ encompasses all of them, notably extending the data volume. ~~The plots show also areas where the synthetic dataset does not have correspondence to in situ data. These areas relate to~~in oligotrophic oceanic waters, that are geographically large but grossly under-sampled. Overall, this figure provides quite robust evidence that the ~~synthetic dataset~~SD has global coverage, from the clearest oceans ~~until~~to all kinds of coastal waters, and that the bio-optical relationships adopted in ~~this~~this study are in line with empirical evidence.

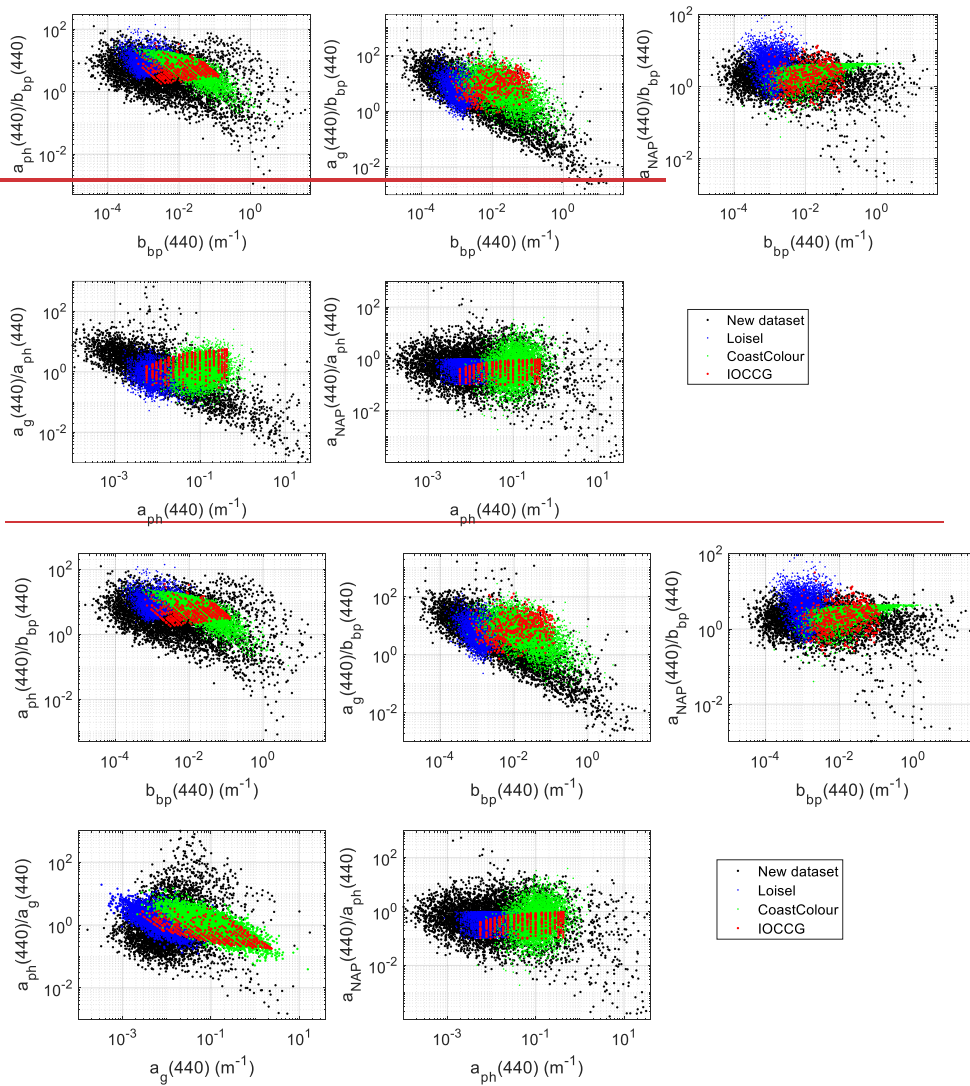


Figure 11: IOP cross-relationship comparison between this and other [synthetic datasetSDs](#).

This [dataset-SD](#) is also compared to the three publicly available [synthetic datasetSDs](#) in Fig. 11: the IOCCG [dataset-SD](#) (IOCCG, 2006), the ~~CoastColour-CoastColour~~ [dataset-SD](#) (Nechad et al., 2015) and Loisel's [dataset-SD](#) (Loisel et al., 2023). ~~The plots highlight that the new dataset covers a much more diverse range of waters than other datasets, acknowledging that such datasets were not aimed at including the widest range of water as this dataset is.~~ Some overlap ~~in the publicly available datasets~~ is noticeable for all crossed IOPs, with Loisel's [dataset-SD](#) more shifted towards clearer waters than IOCCG and ~~CoastColour-CoastColour~~. Also, Loisel's [dataset-SD](#) shows trends that appear more consistent to our [datasetSD](#). ~~As an example,  $\alpha_g(440)/\alpha_{ph}(440)$  appear to show a general decreasing trend with  $\alpha_{ph}(440)$ , corroborated with the in situ datasets. This is well reproduced with Loisel's dataset, whereas the IOCCG dataset shows the opposite trend.~~ The ~~CoastColour-CoastColour~~ [dataset-SD](#) covers the upper part of the range, but due to its optical modelling, many dots are clustered near each other, instead of covering a wider range of values. ~~The new datasetSD covers a wider range of waters than the other datasetSDs combined, a consequence not only of the broad ranges for the OACs, but also of the adequate amount of statistical randomness that was given to the bio-optical relationships.~~

#### **2.24.2 Radiative transfer calculations**

Radiative transfer simulations were made with Hydrolight 5.1.2 (Sequoia Scientific, Inc.). ~~The software was configured with a generic "case 2" water scenario, and the input IOP parameters were set as detailed in section 2.2. Inelastic scattering effects were not considered.~~

Normalized sky radiances were computed using the sky model "HCNRAD" (Harrison and Coombes Normalized RADiances) (Harrison and Coombes, 1988). Diffuse and ~~D~~irect ~~S~~ky irradiances were computed using the "RADTRANX" (RADTRAN eXtended for 300-1000 nm) model (Gregg and Carder, 1990). The ozone concentration was estimated from a climatology derived with binned monthly average TOMS v8 Ozone concentrations (data from 2000-2004 were averaged to give 5-year climatological averages for 5° latitude and 10° longitude quadrants), for the 90<sup>th</sup> day of the year, coordinates 40 ° N and 0 ° E, resulting in 354.9 Dobson units. The US Navy aerosol model was fed with the values: air mass type 5, relative humidity 80.0 %, precipitable water 2.5 cm and horizontal visibility 40.0 km. ~~For the sSea surface roughness was modelled with a Hydrolight-embedded Monte Carlo module, fed with modelling,~~

Field Code Changed

an assumed wind speed of 5.0 m/s ~~was assumed~~. Water index of refraction was calculated as a function of wavelength (Roettgers et al., 2016) for the given seawater T = 20.0 °C and S = 35.0 PSU. The sea was considered vertically homogeneous ~~in depth~~ and infinitely deep.

~~The software~~ IOP input was configured with a generic “case 2” water scenario, ~~and the i~~. Input IOP parameters and phase functions were set as detailed in section 2.2 Table 1. ~~Inelastic scattering effects were not considered~~. Phase functions are a critical component of bio-optical modelling if the angular variability of the light field is considered relevant. Here, ~~p~~Phase functions from the Fournier Forand (FF) family were used both for phytoplankton and for non-algal particles, as they fit very well the angular pattern of measured phase functions. Mobley et al. (2002) documented the indexing of the FF PFs as a function of the backscattering ratio only, a mechanism that is included in Hydrolight parameterized as a function of their respective backscattering ratios. ~~Inelastic scattering effects were not considered~~.

The source code of Hydrolight was modified so that the “printout” output files included reflectances ~~the remote sensing reflectance~~, both above and below the surface, for the whole set of viewing zenith and azimuth angles defined by Hydrolight default quadrants, that is, view angle varying from 0 to 80 ° in steps of 10 ° and then a last value of 87.5° (10 values in total), and azimuth varying from 0 to 180 ° in steps of 15 ° (13 values in total). ~~Then, s~~Simulations were made for the whole range of sun zenith angles defined by the quadrants, that is from 0 to 80 ° in steps of 10 ° and then a last value of 87.5° (10 values in total). Therefore, for every IOP set up, directional AOPs are given at 1300 angles, and non-directional AOPs are given at the 10 sun zenith angles.

#### 940 4.3 (Szeto et al., 2014) Reflectance overview and classification

Synthetic  $R_{rs}$  were scrutinized to ensure that a diverse range of optical water types had been produced. The data underwent partitioning into twelve clusters via a k-means algorithm (Figure. 1242). Ternary plots were employed to visualize the absorption budget for all  $R_{rs}$  within each class, with curves and dots colored based on particle backscattering. This classification is only used here as a method to show the extensive optical diversity within the datasetSD and does not constitute a part of the datasetit.

945 Descriptively, the following water types are:

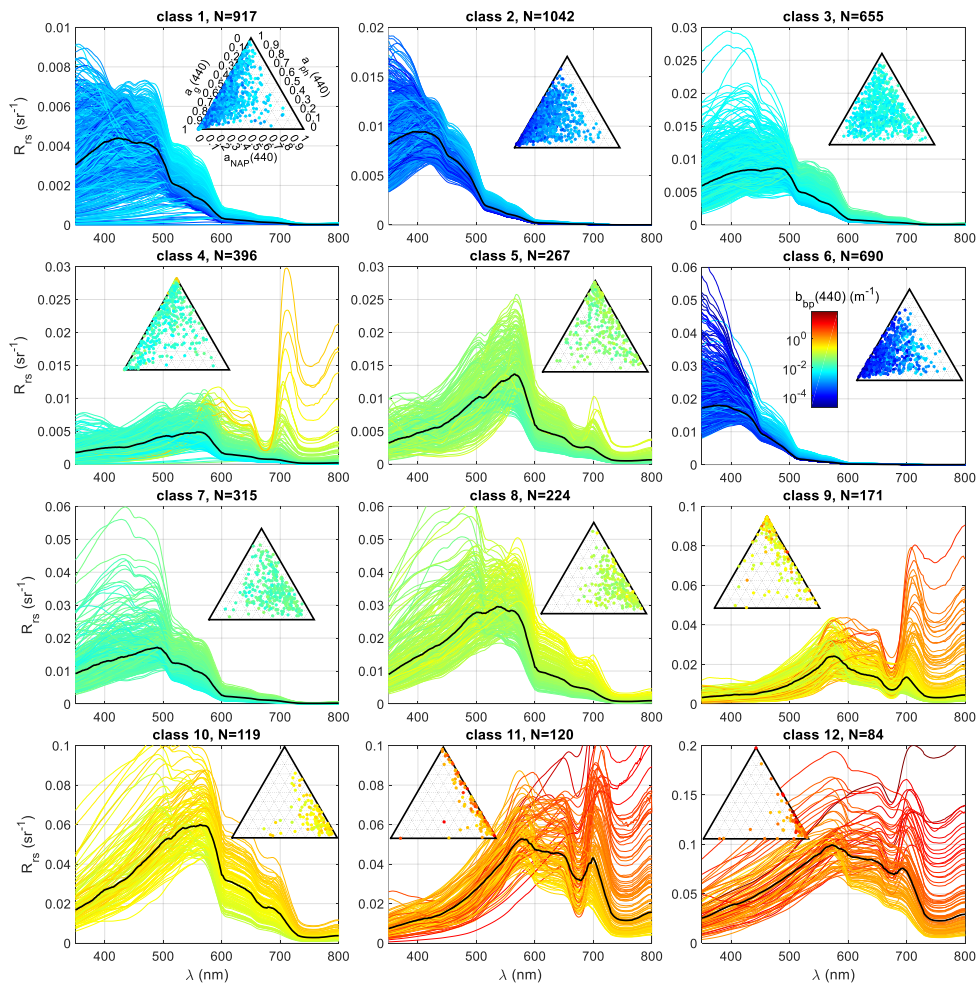
Formatted: English (United States)



### ~~2.3 Reflectance overview and classification~~

~~Synthetic  $R_{rs}$  were scrutinized to ensure that a diverse range of optical water types had been produced. The data underwent partitioning into twelve clusters via a k means algorithm (Figure 12). Ternary plots were employed to visualize the absorption budget for all  $R_{rs}$  within each class, with curves and dots colored based on particle backscattering. This classification is only used here as a method to show the extensive optical diversity within the dataset and does not constitute a part of the dataset. Descriptively, the following water types are:~~

- Classes 2 and 6 relate to clear oceanic waters.
- Class 1 corresponds to highly absorbing waters, with little NAP content.
- Classes 3, 5, 7 and 8 represent coastal waters, exhibiting moderate concentrations of all constituents, in varying proportions.
- Classes 4 and 9 display highly productive waters, marked by high CDOM and NAP levels, respectively.
- Classes 10, 11 and 12 portray highly and very highly turbid waters. Notably, despite categorizing this water type into three classes, their cumulative occurrence is discrete. This outcome stems from the classification, which accentuates disparities in  $R_{rs}$  values that are high.



965 **Figure 12**  $R_{rs}$  spectra (normalized geometry) of the [synthetic dataset SD](#), divided into twelve classes using the k-means classifying algorithm, [with their number \(N\) indicated above](#). Relative to each class, the ternary plots of the absorption budget are plotted. Line and dot color indicates particle backscattering at 440 nm, according to the attached color bar. Note varying vertical scale, across the classes, necessary to visualize the spectral variability across the dynamic ranges.

970 **2.44.4 Angular variation**

Besides the wide IOP ranges, ~~highlighted in the water classes of the following section,~~ a unique characteristic of this [datasetSD](#) is the [inclusion-resolution](#) of the AOPs for the whole range of sun-view geometries. This matter is relevant for algorithm development and validation; for instance, in either in situ or satellite  $R_{rs}$ , the sun is very rarely at the zenith. The view angle is off nadir in above-water platforms and in satellite data, and the azimuth is normally such that avoids the maximum sun glint. This  $R_{rs}$  bidirectionality is very often ignored. Algorithms that use band ratios, such as the oceanic OCx, partially suppress the bidirectional effect because ~~the-its~~ spectral ~~behaviour-pattern~~ is quite flat, but algorithms that rely on the absolute magnitude of  $R_{rs}$  will inevitably propagate bidirectional effects as errors. This section showcases the anisotropy of  $R_{rs}$  for two distinct water types. The first represents very oligotrophic oceanic waters, while the second ~~relates to could correspond to turbid areas with high CDOM, which can be found in shallow marginal seas such as the Azov-Sea~~ [more productive waters](#). The azimuthal angle definition follows that of Hydrolight (i.e., solar photons travel in the  $\phi = 180^\circ$  direction, that is, the sun is located at  $\phi = 0$ ).

A first example of the  $R_{rs}$  anisotropy for a clear water scenario is displayed in Fig. ~~131313~~, for three wavelengths and five sun zenith angles. Related Fig. ~~141414~~ focuses on one sun zenith angle ( $\theta_s = 60^\circ$ ), ~~two the sun's meridian plane ( $\phi = 0, 180^\circ$ ) and its perpendicular vertical plane ( $\phi = -90, 90^\circ$ ), and solar azimuthal planes and~~ a constant zenith view section ( $\theta = 60^\circ$ ), ~~all cases for a reference sun zenith angle ( $\theta_s = 60^\circ$ ).~~ Increasing the sun zenith lowers the azimuthal symmetry and strengthens the radiance anisotropy. A zone of higher values forms along the solar plane for  $\phi = 0$ . It is known that, for very clear waters, the single-scattering approximation can, at least qualitatively, explain the results. The phase functions of both water and particles have a local maximum at [a scattering angle of  \$\Psi = 180^\circ\$](#) , leading to an overall maximum at  $\theta = 60^\circ$ , that is, the back-scattering direction. The secondary maximum at  $\theta = -60^\circ$  (or  $\theta = 60^\circ$  for  $\phi = 180^\circ$ ) can be explained by the balance between [a](#) progressive increase in the particle phase function and [a](#) decrease in the water phase function as  $\Psi$  decreases.

Formatted: Font: (Default) Times New Roman, 12 pt, English (United States), Check spelling and grammar

Formatted: Font: (Default) Times New Roman, 12 pt, English (United States), Check spelling and grammar

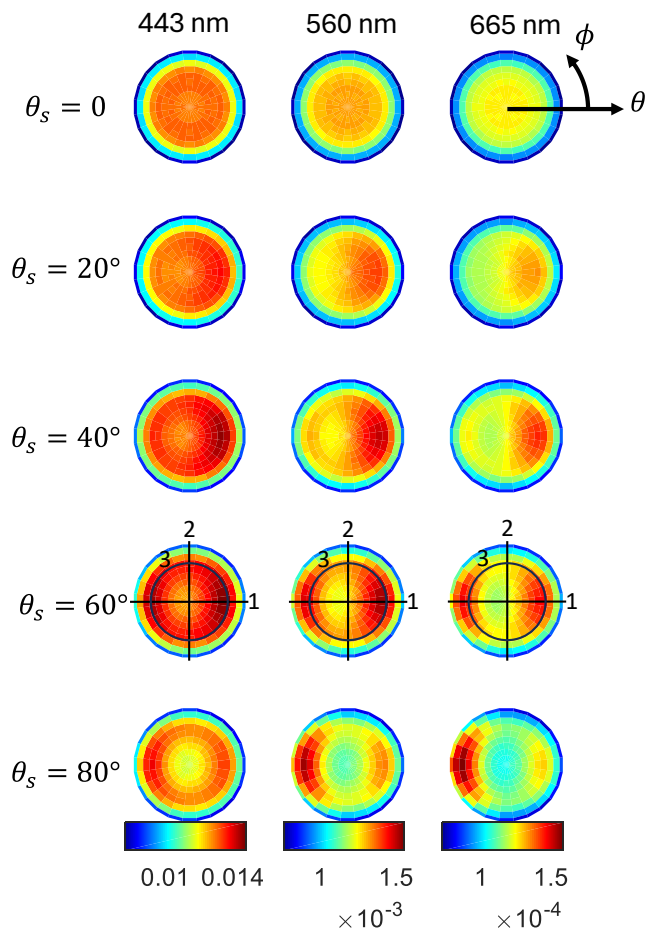
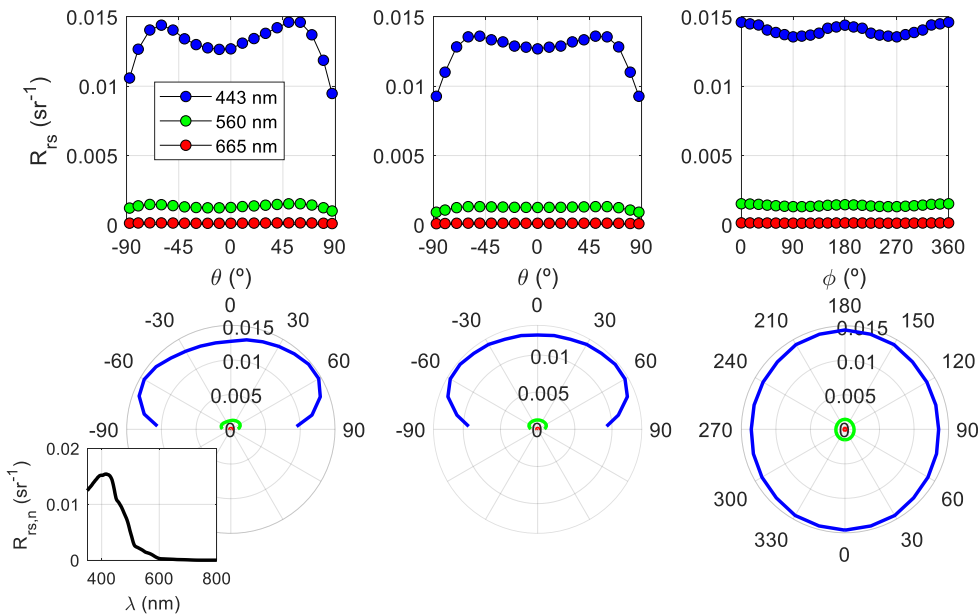


Figure 131313 Angular variability of  $R_{rs}$  for the oligotrophic water spectrum shown in Figure. 141414. The polar plots are divided into selected sun zenith angles (rows) and wavelengths (columns). The polar angle represents the azimuth (zero “looking at the sun”), while the radius represents the radiance propagation angle (same as the viewing zenith angle). The color represents the  $R_{rs}$  magnitude. The color scale among wavelengths for visualization purposes. For  $\theta_s=60^\circ$  specifically, some indicated slices are presented in 1D plots in Figure. 141414. Section 1: sun’s meridian plane. Section 2: perpendicular plane to the sun’s meridian plane. Section 3: constant  $\theta=60^\circ$ .



1005 **Figure 14144** Angular variability of Hydrolight-simulated  $R_{rs}$  for the oligotrophic water case (spectrum shown in a corner). The plots represent the three sections for  $\theta_s=60^\circ$  in Figure. 131313, in consecutive columns. Here, the sections are plotted in cartesian coordinates in the upper plots and polar coordinates in the lower ones.

1010 Figures. 151515 and 161616 show an analog example for a turbid-productive water scenario. Notable is the azimuthal maximum shifts to the  $\phi = 180^\circ$  direction. This is explained by the dominance of the particle phase function and the appearance of multiple scattering, which starts to become important even for small concentrations. This implies that the radiance at angle  $\theta = -70^\circ$  (or  $\theta = 70^\circ$  for  $\phi = 180^\circ$ ) is less influenced by the shape of the phase function at the particular direction given by the single scattering direction. Instead, multiple scattering ~~does not randomize the light field in all directions, making it isotropic, but instead,~~ makes the resulting radiances influenced by the phase function in variable ranges reaching  $\Psi < 120^\circ$ , where it increases sharply. ~~Indeed, multiple scattering does not generate isotropy in  $R_{rs}$  as might be believed by some, but instead changes the angular pattern of the anisotropy.~~

Formatted: Font: (Default) Times New Roman, 12 pt, English (United States), Check spelling and grammar

Formatted: Font: (Default) Times New Roman, 12 pt, English (United States), Check spelling and grammar

This behaviour, although ~~was~~ already documented (Loisel and Morel, 2001), ~~but it~~ was somehow not assimilated by most within the community.

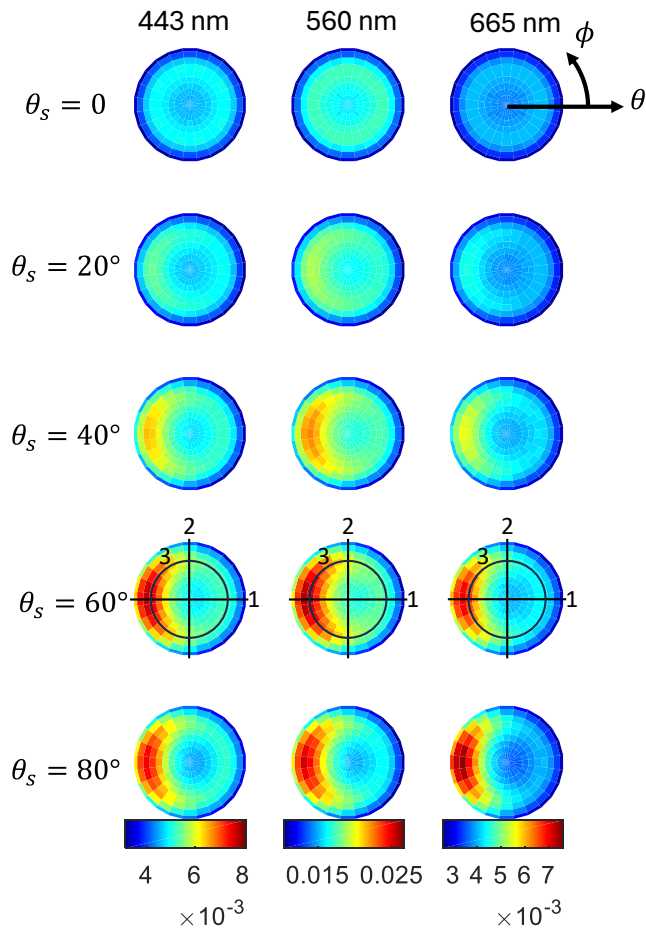


Figure 151515 As in [Figure 17](#)[Figure 13](#) [Fig. 13](#), but for the angular variability of  $R_{rs}$  for the **turbid productive waters** case.

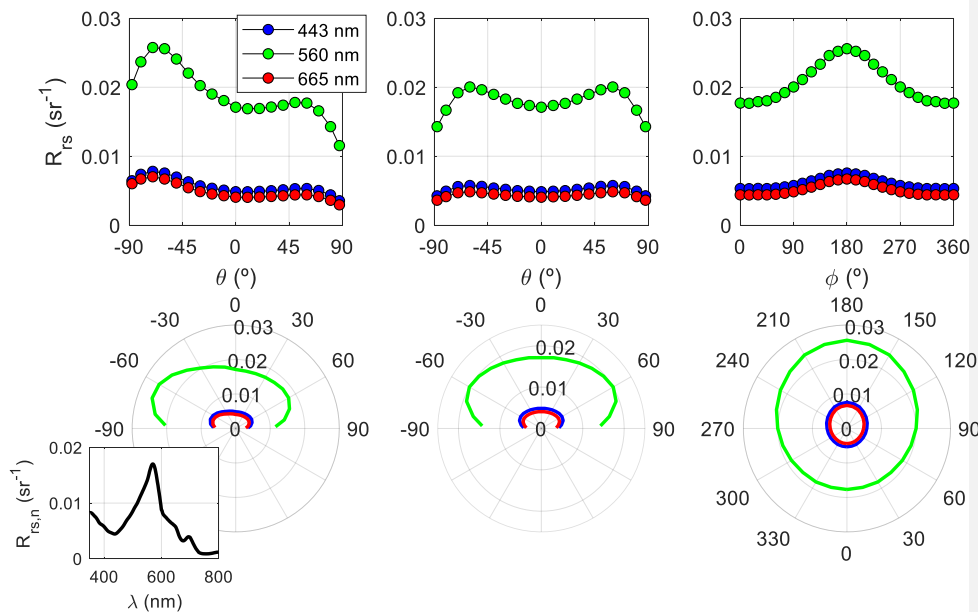


Figure 161616 As in [Figure 17](#)[Figure 13](#) [Fig. 1414](#), but for the angular variability of  $R_{rs}$  for the **turbid productive waters** case.

#### 4.5 Reflectance validation with in situ data

The number of relationships imposed to the IOPs, as well as the cross-checks among them give confidence on the realism of the [datasetSD](#) generated. Yet, to be further confident that the synthetic AOPs represent natural waters, it is desirable to show some [evidence-comparison to in situ data](#) that involves the AOPs themselves.

We evaluated in [Fig. 1747](#) the  $R_{rs}$  (normalized geometry) of our entire [synthetic-datasetSD](#) through the spectral quality index (QWIP) by Dierssen et al. (2022). Such index aims at providing a quality estimate for a hyperspectral  $R_{rs}$ . QWIP was developed a large dataset of in situ  $R_{rs}$ , so this comparison is indirectly

Formatted: Font: 12 pt, English (United States), Check spelling and grammar

1040 actually can be seen as a comparison with to real  $R_{rs}$  data. In Dierssen et al. (2022), it is mentioned that values within the 0.2 margins have high similarity to real spectra measured in the field, which for the case of the SD, is verified in are all 4993 out of the 5000 but 7 spectra. Still, these 7 spectra are close to the limit, and may simply contain some bio-optical characteristics, that were not present in the QWIP calibration dataset. No spectra are clearly off from the main trend line, thus giving confidence in the quality of our dataset SD in terms of this index and of the data from which it was derived.

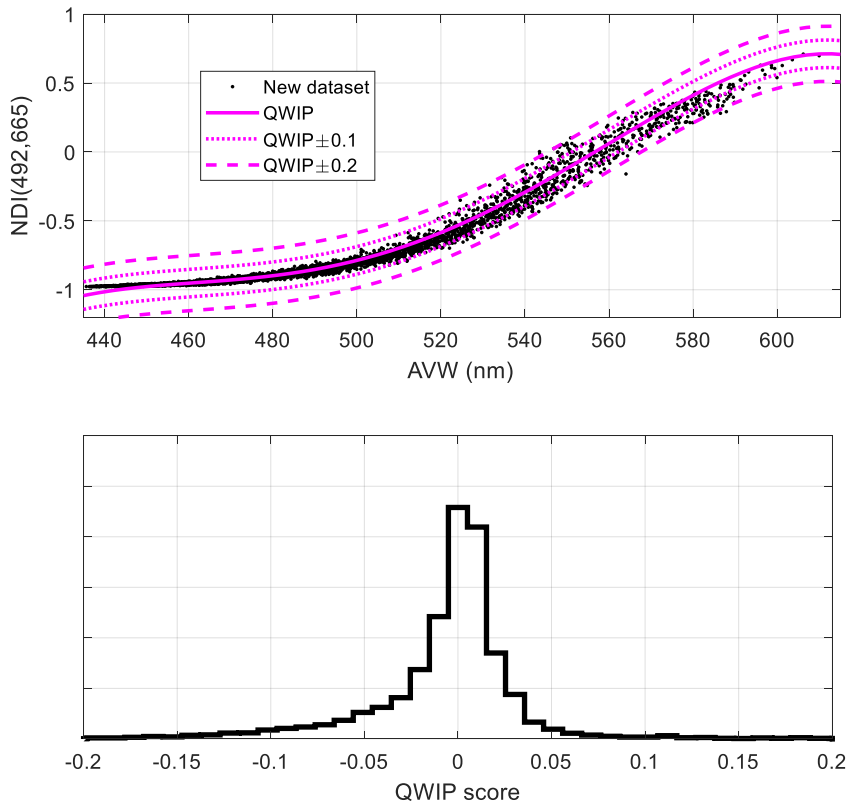


**Figure 1747** Upper plot: scatter plot between the apparent optical wavelength (Vandermeulen et al., 2020) and the NDI index:  $NDI(492, 665) = \frac{R_{rs}(665) - R_{rs}(492)}{R_{rs}(665) + R_{rs}(492)}$ . Magenta lines: QWIP score (Dierssen et al., 2022)



1045 and error bars. Lower plot: histogram of the QWIP score, defined as the difference respect to the QWIP curve.

Next assessment helps to verify the covariability between  $R_{rs}$  and the absorption coefficient. A one-dimensional predictor  $\chi$  is derived from an  $R_{rs}$  (Lee et al., 2002), as in eq. (132019):

$$\chi = \log_{10} \left( \frac{R_{rs}(443) + R_{rs}(490)}{R_{rs}(560) + 5 \frac{R_{rs}^2(665)}{R_{rs}(490)}} \right) \cdot (2019)$$

1050 This  $\chi$  index is matched to non-water absorption spectrum at 560 nm  $a_{nw}(560)$ . There are several open access, freely available in situ datasets that contain both measured variables matched together, such as Valente et al. (2022), Zibordi and Berthon (2024) and the PACE Schaeffer, Mouw and Biosope datasets (Casey et al., 2020). Figure. 1818 clearly shows the excellent average overlap between our synthetic datasetSD and measured data, besides differences due to the difficulties of measuring very low absorption.

1055 Different bio-optical characteristics produce slight deviations from the mean curvetrend, indicating natural variability.

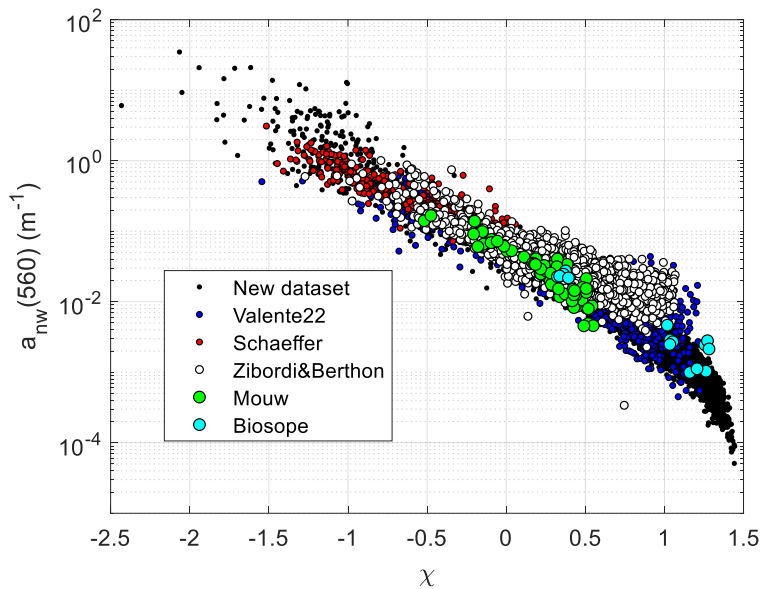


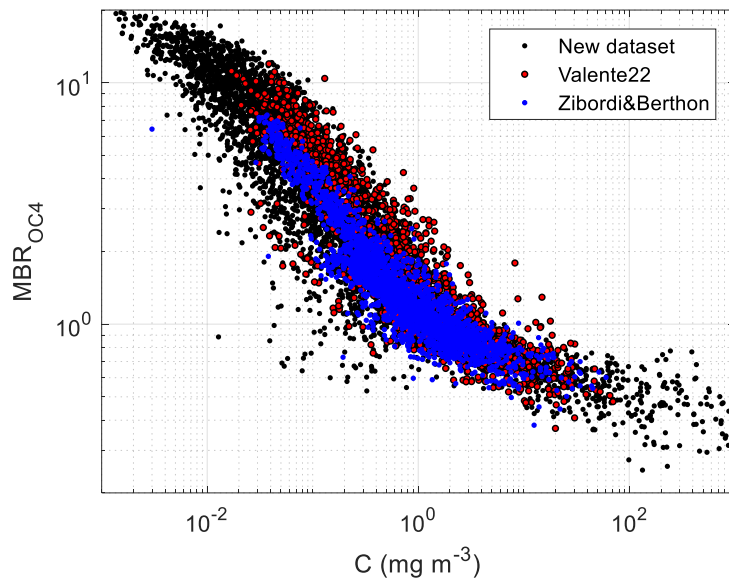
**Figure 1818** A scatter plot between the  $R_{rs}$ -generated  $\chi$  index and the matched non-water absorption spectrum at 560 nm,  $a_{nw}(560)$ . Black dots are from the synthetic datasetSD and coloured dots are from field data from various references (see text).

A typical benchmark is shown next, where a given chlorophyll concentration in the datasetSD is related to the generated  $R_{rs}$  through the maximum band ratio  $MBR_{OC4}$ , an index that is used to estimate chlorophyll in the ocean, defined in eq. (2120):

$$MBR_{OC4} = \frac{\max [R_{rs}(443), R_{rs}(490), R_{rs}(510)]}{R_{rs}(560)} \quad (2120)$$

This index has been also used to study the consistency of a given datasetSD in all kinds of water (Nechad et al., 2015). Here, matched  $MBR_{OC4}$  and chlorophyll concentration from two large in situ datasets are plotted (Valente et al., 2022; Zibordi and Berthon, 2024), showing a good general overlap, though with some degree of differences among them, that are explainable due to different bio-optical characteristics of the seas sampled (Szeto et al., 2011). Data from our datasetSD generally agrees with the trend, that essentially shows high linearity in the middle section, while saturating at the extremes due to loss of

sensitivity. The data cloud of the [synthetic datasetSD](#) also displays a spread that embraces the in situ datasets used for comparison, suggesting that the optical variability in the in situ datasets is well represented.



1075 **Figure 1949** Chlorophyll concentration as a function of the maximum band ratio for OC4-type algorithms, for the [synthetic datasetSD](#) and for data in Valente et al. (2022) and Zibordi and Berthon (2024).

The last comparison to real  $R_{rs}$  data involves the relationship to the total suspended matter concentration ( $T$ ), a relevant parameter for coastal and inland water studies, which usually show higher turbidities. Interestingly, this involves the absolute value of  $R_{rs}$  and not ratios. In particular, it is known that  $T$  covaries with  $R_{rs}$  at long wavelengths, and 665 nm is commonly employed, due to the lesser disturbance by CDOM. Our [datasetSD](#) does not use  $T$  for its generation, so the estimation  $T = N + 0.07C$ , after Brando and Dekker (2003). [Figure. 2020](#) shows that the new [datasetSD](#) follows the same trend as that includes that in from in situ datasets (Valente et al., 2022; Zibordi and Berthon, 2024), but also displaying

1080

1085 a level of spread that includes the in situ datasets, once more demonstrating the success in reproducing a range of natural variability.

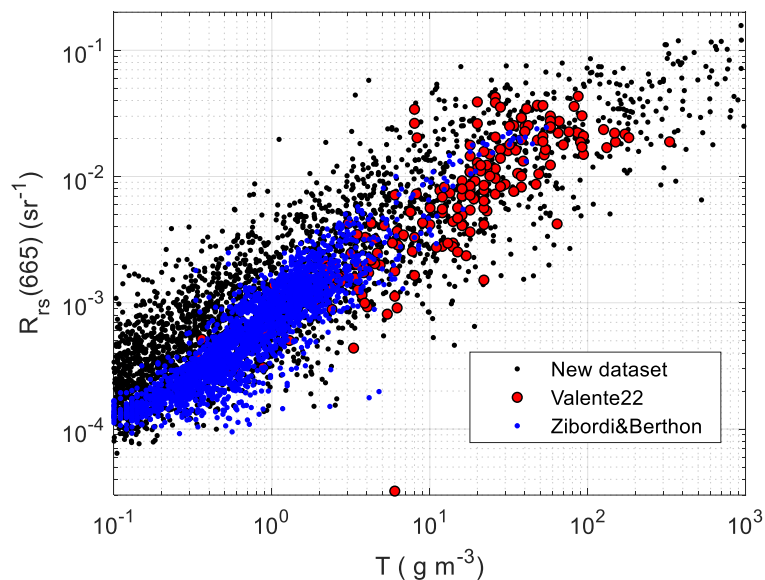


Figure 2020 Total suspended matter concentration as a function of  $R_{rs}(665)$ , for the synthetic datasetSD and for data in Valente et al. (2022) and Zibordi and Berthon (2024).

Formatted: Normal

### 1090 3.5. Data file description

Output data is organized in netCDF files, where each file contains a given IOP setup and all directional AOP output. Table 4 details the content of the file structure. Variables have different sizes, according to their dependence on the following variables that can take the following number of different values: sun zenith angle  $\theta_s, n_s = 10$ , zenithal direction of radiance propagation,  $\theta, n_\theta = 10$ , azimuthal direction of radiance propagation  $\phi, n_\phi = 13$ , wavelength of radiation in vacuum  $\lambda, n_\lambda = 451$ . All in-water AOPs refer to the zero depth, just below the surface. Diffuse attenuation coefficients instead required the

choice of two depths approximate the depth derivatives, which were 0 m and 1 cm, as set by default in Hydrolight.

**Table 4 File description**

Parameter	Description	Units	Size
C	Chlorophyll concentration	mg m <sup>-3</sup>	1 x 1
N	Non-algal particles concentration	g m <sup>-3</sup>	1 x 1
Y	Light absorption coefficient of coloured dissolved organic matter at 440 nm	m <sup>-1</sup>	1 x 1
theta_s	Sun zenith angle (zero at zenith)	°	n <sub>s</sub> x 1
theta	Zenithal direction of radiance propagation (zero towards zenith)	°	n <sub>θ</sub> x 1
phi	Azimuthal direction of radiance propagation (zero towards the sun)	°	n <sub>φ</sub> x 1
lambda	Wavelength of radiation in vacuum	nm	n <sub>λ</sub> x 1
Esdire_Es_ratio	Above-surface direct to total downwelling irradiance ratio	-	n <sub>s</sub> x n <sub>λ</sub>
aw	Spectral light absorption coefficient by seawater at 20 °C and S=35 PSU	m <sup>-1</sup>	n <sub>λ</sub> x 1
aph	Spectral light absorption coefficient by phytoplankton	m <sup>-1</sup>	n <sub>λ</sub> x 1
ay	Spectral light absorption coefficient by coloured dissolved organic matter	m <sup>-1</sup>	n <sub>λ</sub> x 1
aNAP	Spectral light absorption coefficient by non-algal particles	m <sup>-1</sup>	n <sub>λ</sub> x 1
bw	Spectral light scattering coefficient by seawater at 20 °C and S=35 PSU	m <sup>-1</sup>	n <sub>λ</sub> x 1

bph	Spectral light scattering coefficient by phytoplankton	$m^{-1}$	$n_{\lambda} \times 1$
bNAP	Spectral light scattering coefficient by non-algal particles	$m^{-1}$	$n_{\lambda} \times 1$
bbw	Spectral light backscattering coefficient by seawater at 20 °C and S=35 PSU	$m^{-1}$	$n_{\lambda} \times 1$
bbph	Spectral light backscattering coefficient by phytoplankton	$m^{-1}$	$n_{\lambda} \times 1$
bbNAP	Spectral light backscattering coefficient by non-algal particles	$m^{-1}$	$n_{\lambda} \times 1$
Rrs	Spectral angle-dependent above-water remote sensing reflectance $\left(\frac{L_w}{E_s}\right)$	$sr^{-1}$	$n_s \times n_{\theta} \times n_{\phi} \times n_{\lambda}$
rrs	Spectral angle-dependent underwater radiance reflectance $\left(\frac{L_u}{E_d}\right)$	$sr^{-1}$	$n_s \times n_{\theta} \times n_{\phi} \times n_{\lambda}$
Q	Spectral angle-dependent underwater Q-factor $\left(\frac{E_u}{L_u}\right)$	sr	$n_s \times n_{\theta} \times n_{\phi} \times n_{\lambda}$
Kou	Spectral diffuse attenuation coefficient of scalar upwelling irradiance	$m^{-1}$	$n_s \times n_{\lambda}$
Kod	Spectral diffuse attenuation coefficient of scalar downwelling irradiance	$m^{-1}$	$n_s \times n_{\lambda}$
Ko	Spectral diffuse attenuation coefficient of scalar total (spherical) irradiance	$m^{-1}$	$n_s \times n_{\lambda}$
Ku	Spectral diffuse attenuation coefficient of planar upwelling irradiance	$m^{-1}$	$n_s \times n_{\lambda}$
Kd	Spectral diffuse attenuation coefficient of planar downwelling irradiance	$m^{-1}$	$n_s \times n_{\lambda}$

Knet	Spectral diffuse attenuation coefficient of net planar irradiance	$m^{-1}$	$n_s \times n_\lambda$
KLu	Spectral diffuse attenuation coefficient of upwelling radiance towards the zenith	$m^{-1}$	$n_s \times n_\lambda$
mu_u	Spectral average cosine of the upwelling radiance	-	$n_s \times n_\lambda$
mu_d	Spectral average cosine of the downwelling radiance	-	$n_s \times n_\lambda$
mu_tot	Spectral average cosine of the total radiance	-	$n_s \times n_\lambda$
R	Spectral underwater irradiance reflectance $\left(\frac{E_u}{E_d}\right)$	-	$n_s \times n_\lambda$

#### 4.6. Data availability

Data described in this manuscript ~~can be accessed~~ freely accessible at ~~from~~ Zenodo ~~under at~~ <https://doi.org/10.5281/zenodo.11637178> ~~https://zenodo.org/records/11637178~~ (Pitarch and Brando, 2024). The repository hosts two versions of the dataset: one hyperspectral, from 350 nm to 900 nm, in steps of 1 nm, and a smaller, multispectral one, for the twelve Sentinel 3-OLCI bands between 400 nm and 753 nm.

#### 5.7. Conclusions

~~With the development of the presented synthetic dataset, encompassing inherent and apparent optical properties alongside associated optically active constituents, we believe to have~~The presented dataset ~~filled-fills~~ several gaps, as identified in our literature review of publicly available in situ and synthetic datasets. ~~On one hand, t~~The large quantity and high quality of the in situ data allowed the application of stringent quality control procedures to develop novel bio-optical relationships involving parameters that model absorption and scattering of the optically active constituents. The spread in the data clouds used for bio-optical modelling was reproduced as probability density functions, resulting in a realistic depiction

1115 ~~in the synthetic dataset~~ of the natural variability of the in situ data. Validation exercises were provided for the remote-sensing reflectance, showing consistency with the benchmark in situ datasets for every example. Our dataset is therefore representative of natural waters of varying trophic levels and optical complexity. ~~As a by-product of the~~ ~~the reported~~ The underlying bio-optical relationships can be assumed to become a reference for future optical studies.

1120 Apparent optical properties are resolved at all geometric angles available by the radiative transfer simulations, making this one the first directional dataset ever published. This detail makes it suitable for directional studies of reflectance, diffuse attenuation and any other derived quantity. The dataset, in its hyperspectral and multi-angular format, is relevant for bio-optical and directional studies applied to current satellite-borne sensors such as OLCI, and as well as to next-generation missions like such as PACE and CHIME.

1125 The synthetic dataset is distributed in ~~the standard format~~ netCDF format as single files for every IOP case, files as it is enabling efficient-convenient for data storage and space management, as well as straightforward handling with software packages. ~~Given~~ ~~Despite~~ the very fine spectral ~~resolution step~~ of 1 nm between 350 nm and 800 nm and that each file contains the IOP setup as well as all directional AOPs for all 1300 angular configurations (and hemispheric variables such as  $K_d$  are included for all 10 sun zenith angles), each of the 5000 files only weights approximately 5700 kB. ~~The netCDF format also makes the dataset easy to handle using common software packages.~~

1130

### 6.8. Author contribution

J.P., V.E.B: Conceptualization of the study, development or design of methodology, validation, Writing – review & editing. J.P.: Data curation, Formal analysis, Software, Visualization, Writing – original draft preparation. V.E.B.: Funding acquisition, Project administration.

1135

### 7.9. Competing interests

The authors declare that they have no conflict of interest.



## **8.10. Acknowledgements**

We are grateful to Davide d'Alimonte, Tamito Kajiyama, Constant Mazeran and Marco Talone for carrying out independent analyses with previous versions of this dataset, that were fundamental to develop it to its final configuration. Flavio la Padula and Vega Forneris assisted with IT requirements. Curtis Mobley, Juan Ignacio Gossn, Giuseppe Zibordi, David McKee and Reviewer 1 are thanked for proving valuable comments and suggestions on a previous version of the manuscript that helped to improve its quality.

This study was carried out in the frame of the Copernicus study “BRDF correction of S3 OLCI water reflectance products” (contract No.RB\_EUM-CO-21-4600002626-JIG), conducted by EUMETSAT. The work also acknowledges the support of the Ocean Colour Thematic Assembly Centre of the Copernicus Marine Environment and Monitoring Service (contract: 21001L02-COP-TAC OC-2200–Lot 2: Provision of Ocean Colour Observation Products (OC-TAC)). J.P. thanks financial support by the EU - Next Generation EU Mission 4 “Education and Research” - Project IR0000032 – ITINERIS - Italian Integrated Environmental Research Infrastructures System - CUP B53C22002150006.

## **References**

Astoreca, R., Doxaran, D., Ruddick, K., Rousseau, V., and Lancelot, C.: Influence of suspended particle concentration, composition and size on the variability of inherent optical properties of the Southern North Sea, *Continental Shelf Research*, 35, 117-128, <https://doi.org/10.1016/j.csr.2012.01.007>, 2012.

Aurin, D. A., Dierssen, H. M., Twardowski, M. S., and Roesler, C. S.: Optical complexity in Long Island Sound and implications for coastal ocean color remote sensing, *Journal of Geophysical Research: Oceans*, 115, <https://doi.org/10.1029/2009JC005837>, 2010.

Babin, M., Stramski, D., Ferrari, G. M., Claustre, H., Bricaud, A., Obolensky, G., and Hoepffner, N.: Variations in the light absorption coefficients of phytoplankton, nonalgal particles, and dissolved organic matter in coastal waters around Europe, *Journal of Geophysical Research: Oceans*, 108, <https://doi.org/10.1029/2001JC000882>, 2003.

- Bengil, F., McKee, D., Beşiktepe, S. T., Sanjuan Calzado, V., and Trees, C.: A bio-optical model for integration into ecosystem models for the Ligurian Sea, *Progress in Oceanography*, 149, 1-15, 1165 <https://doi.org/10.1016/j.pocean.2016.10.007>, 2016.
- Bernard, S., Probyn, T. A., and Quirantes, A.: Simulating the optical properties of phytoplankton cells using a two-layered spherical geometry, *Biogeosciences Discuss.*, 2009, 1497-1563, 10.5194/bgd-6-1497-2009, 2009.
- Blondeau-Patissier, D., Brando, V. E., Oubelkheir, K., Dekker, A. G., Clementson, L. A., and Daniel, P.: 1170 Bio-optical variability of the absorption and scattering properties of the Queensland inshore and reef waters, Australia, *Journal of Geophysical Research: Oceans*, 114, <https://doi.org/10.1029/2008JC005039>, 2009.
- Blondeau-Patissier, D., Schroeder, T., Clementson, L. A., Brando, V. E., Purcell, D., Ford, P., Williams, D. K., Doxaran, D., Anstee, J., Thapar, N., and Tovar-Valencia, M.: Bio-Optical Properties of Two 1175 Neighboring Coastal Regions of Tropical Northern Australia: The Van Diemen Gulf and Darwin Harbour, *Front. Mar. Sci.*, 4, 10.3389/fmars.2017.00114, 2017.
- Bracher, A.: Phytoplankton pigment concentrations in the Southern Ocean during RV POLARSTERN cruise PS103 in Dec 2016 to Jan 2017. In: Supplement to: Álvarez, Eva; Thoms, Silke; Bracher, Astrid; Liu, Y; Völker, Christoph (2019): Modeling Photoprotection at Global Scale: The Relative Role of 1180 Nonphotosynthetic Pigments, Physiological State, and Species Composition. *Global Biogeochemical Cycles*, 33(7), 904-926, <https://doi.org/10.1029/2018GB006101>, PANGAEA, 2019.
- Bracher, A., and Liu, Y.: Spectrophotometric measurements of absorption coefficients by non-algal particles in the Atlantic Southern Ocean during RV POLARSTERN cruise PS103 in Dec 2016 to Jan 2017. PANGAEA, 2021.
- 1185 Bracher, A., Liu, Y., Hellmann, S., and Röttgers, R.: Absorption coefficients by coloured dissolved organic matter from North Sea to Fram Strait measured underway with a Liquid Waveguide Capillary Cell system during POLARSTERN cruise PS99.1. PANGAEA, 2021a.

- 1190 Bracher, A., Liu, Y., Oelker, J., and Röttgers, R.: Absorption coefficients by coloured dissolved organic matter across the South Atlantic Ocean measured underway with a Liquid Waveguide Capillary Cell system during POLARSTERN cruise PS103. PANGAEA, 2021b.
- Bracher, A., Liu, Y., and Wiegmann, S.: Spectrophotometric measurements of absorption coefficients by phytoplankton during HEINCKE cruise HE462 in the North Sea and Sogne Fjord from 29 April to 7 May 2016. PANGAEA, 2021c.
- 1195 Bracher, A., Liu, Y., and Wiegmann, S.: Spectrophotometric measurements of absorption coefficients by non-algal particles during during HEINCKE cruise HE462 in the North Sea and Sogne Fjord from 29 April to 7 May 2016. PANGAEA, 2021d.
- Bracher, A., Liu, Y., and Wiegmann, S.: Spectrophotometric measurements of absorption coefficients by non-algal particles during RV POLARSTERN cruise PS121 from 11 Aug to 10 Sep 2019. PANGAEA, 2021e.
- 1200 Bracher, A., Liu, Y., and Wiegmann, S.: Spectrophotometric measurements of absorption coefficients by phytoplankton during RV POLARSTERN cruise PS121 from 11 Aug to 10 Sep 2019. PANGAEA, 2021f.
- Bracher, A., Liu, Y., Wiegmann, S., and Röttgers, R.: Absorption coefficients by coloured dissolved organic matter obtained underway with a Liquid Waveguide Capillary Cell system during HEINCKE cruise HE462 in the North Sea and Sogne Fjord. PANGAEA, 2021g.
- 1205 Bracher, A., Liu, Y., Wiegmann, S., and Röttgers, R.: Absorption coefficients by coloured dissolved organic matter (CDOM) from North Sea to Fram Strait measured at fixed stations with a Liquid Waveguide Capillary Cell system during POLARSTERN cruise PS121. PANGAEA, 2021h.
- Bracher, A., Liu, Y., Wiegmann, S., Xi, H., and Röttgers, R.: Absorption coefficients by coloured dissolved organic matter across the Atlantic Ocean measured underway with a Liquid Waveguide  
1210 Capillary Cell system during POLARSTERN cruise PS113. PANGAEA, 2021i.

Bracher, A., Liu, Y., Xi, H., and Wiegmann, S.: Spectrophotometric measurements of absorption coefficients by non-algal particles during POLARSTERN cruise PS113 along an Atlantic Transect. PANGAEA, 2021j.

1215 Bracher, A., Liu, Y., Xi, H., and Wiegmann, S.: Spectrophotometric measurements of absorption coefficients by phytoplankton during POLARSTERN cruise PS113 along an Atlantic Transect. PANGAEA, 2021k.

Bracher, A., and Taylor, B. B.: Phytoplankton absorption during POLARSTERN cruise ANT-XXVI/4 (PS75). PANGAEA, 2021.

1220 Bracher, A., Taylor, B. B., and Cheah, W.: Phytoplankton absorption during SONNE cruise SO218. PANGAEA, 2021l.

Brando, V. E., and Dekker, A. G.: Satellite hyperspectral remote sensing for estimating estuarine and coastal water quality, *IEEE Transactions on Geoscience and Remote Sensing*, 41, 1378-1387, 10.1109/TGRS.2003.812907, 2003.

1225 Brando, V. E., Dekker, A. G., Park, Y. J., and Schroeder, T.: Adaptive semianalytical inversion of ocean color radiometry in optically complex waters, *Applied Optics*, 51, 2808-2833, 10.1364/AO.51.002808, 2012.

Brewin, R. J. W., Dall'Olmo, G., Sathyendranath, S., and Hardman-Mountford, N. J.: Particle backscattering as a function of chlorophyll and phytoplankton size structure in the open-ocean, *Opt. Express*, 20, 17632-17652, 10.1364/OE.20.017632, 2012.

1230 Bricaud, A., Babin, M., Morel, A., and Claustre, H.: Variability in the chlorophyll-specific absorption coefficients of natural phytoplankton: Analysis and parameterization, *J. Geophys. Res.*, 100, 13321, 10.1029/95JC00463, 1995.

- 1235 Bricaud, A., Morel, A., Babin, M., Allali, K., and Claustre, H.: Variations of light absorption by  
suspended particles with chlorophyll *a* concentration in oceanic (case 1) waters: Analysis and  
implications for bio-optical models, *Journal of Geophysical Research: Oceans*, 103, 31033-31044,  
10.1029/98JC02712, 1998.
- 1240 Casey, K. A., Rousseaux, C. S., Gregg, W. W., Boss, E., Chase, A. P., Craig, S. E., Mouw, C. B.,  
Reynolds, R. A., Stramski, D., Ackleson, S. G., Bricaud, A., Schaeffer, B., Lewis, M. R., and Maritorea,  
S.: A global compilation of in situ aquatic high spectral resolution inherent and apparent optical property  
data for remote sensing applications, *Earth Syst. Sci. Data*, 12, 1123-1139, 10.5194/essd-12-1123-2020,  
2020.
- 1245 Castagna, A., Amadei Martínez, L., Bogorad, M., Daveloose, I., Dasseville, R., Dierssen, H. M., Beck,  
M., Mortelmans, J., Lavigne, H., Dogliotti, A., Doxaran, D., Ruddick, K., Vyverman, W., and Sabbe, K.:  
Optical and biogeochemical properties of diverse Belgian inland and coastal waters, *Earth Syst. Sci. Data*,  
14, 2697-2719, 10.5194/essd-14-2697-2022, 2022.
- Chami, M., Lafrance, B., Fougnie, B., Chowdhary, J., Harmel, T., and Waquet, F.: OSOAA: a vector  
radiative transfer model of coupled atmosphere-ocean system for a rough sea surface application to the  
estimates of the directional variations of the water leaving reflectance to better process multi-angular  
satellite sensors data over the ocean, *Opt. Express*, 23, 27829-27852, 10.1364/OE.23.027829, 2015.
- 1250 Cherukuru, N., Davies, P. L., Brando, V. E., Anstee, J. M., Baird, M. E., Clementson, L. A., and Doblin,  
M. A.: Physical oceanographic processes influence bio-optical properties in the Tasman Sea, *Journal of  
Sea Research*, 110, 1-7, <https://doi.org/10.1016/j.seares.2016.01.008>, 2016.
- 1255 Churilova, T., Moiseeva, N., Skorokhod, E., Efimova, T., Buchelnikov, A., Artemiev, V., and Salyuk, P.:  
Parameterization of Light Absorption of Phytoplankton, Non-Algal Particles and Coloured Dissolved  
Organic Matter in the Atlantic Region of the Southern Ocean (Austral Summer of 2020), *Remote Sensing*,  
15, 634, 2023.

D'Alimonte, D., Zibordi, G., Kajiyama, T., and Cunha, J. C.: Monte Carlo code for high spatial resolution ocean color simulations, *Applied Optics*, 49, 4936-4950, 10.1364/AO.49.004936, 2010.

1260 Dierssen, H. M., Vandermeulen, R. A., Barnes, B. B., Castagna, A., Knaeps, E., and Vanhellefont, Q.: QWIP: A Quantitative Metric for Quality Control of Aquatic Reflectance Spectral Shape Using the Apparent Visible Wavelength, *Frontiers in Remote Sensing*, 3, 10.3389/frsen.2022.869611, 2022.

Doerffer, R., and Schiller, H.: The MERIS Case 2 water algorithm, *International Journal of Remote Sensing*, 28, 517-535, 10.1080/01431160600821127, 2007.

1265 Fournier, G. R., and Forand, J. L.: Analytic phase function for ocean water, *Ocean Optics XII*, 1994, 194-201,

Gonçalves-Araujo, R., Wiegmann, S., and Bracher, A.: Absorption coefficient spectra of non-algal particles during POLARSTERN cruise ARK-XXVI/3 (PS78, TRANSARC). In: In supplement to: Gonçalves-Araujo, Rafael; Rabe, Benjamin; Peeken, Ilka; Bracher, Astrid (2018): High colored dissolved organic matter (CDOM) absorption in surface waters of the central-eastern Arctic Ocean: Implications for biogeochemistry and ocean color algorithms. *PLoS ONE*, 13(1), e0190838, <https://doi.org/10.1371/journal.pone.0190838>, PANGAEA, 2018.

Gons, H. J., Burger-Wiersma, T., Otten, J. H., and Rijkeboer, M.: Coupling of phytoplankton and detritus in a shallow, eutrophic lake (Lake Loosdrecht, The Netherlands), in: *Restoration and Recovery of Shallow Eutrophic Lake Ecosystems in The Netherlands*, Dordrecht, 1992, 51-59,

1275 Gregg, W. W., and Carder, K. L.: A simple spectral solar irradiance model for cloudless maritime atmospheres, *Limnol. Oceanogr.*, 35, 1657-1675, 10.4319/lo.1990.35.8.1657, 1990.

Harrison, A. W., and Coombes, C. A.: Angular distribution of clear sky short wavelength radiance, *Solar Energy*, 40, 57-63, 1988.

- He, S., Zhang, X., Xiong, Y., and Gray, D.: A Bidirectional Subsurface Remote Sensing Reflectance  
1280 Model Explicitly Accounting for Particle Backscattering Shapes, *Journal of Geophysical Research: Oceans*, 122, 8614-8626, 10.1002/2017JC013313, 2017.
- Hölemann, J. A., Koch, B. P., Juhls, B., and Timokhov, L.: Colored dissolved organic matter (CDOM) and dissolved organic carbon (DOC) measured during cruise TRANSDRIFT-XXII, Laptev Sea. PANGAEA, 2020.
- 1285 IOCCG: Remote Sensing of Inherent Optical Properties: Fundamentals, Tests of Algorithms, and Applications, International Ocean-Colour Coordinating Group, IOCCG, Dartmouth, Canada5, 1-122, 2006.
- Juhls, B., Kattner, G., and Skorospekhova, T.: Surface water Dissolved Organic Matter (CDOM) in the Lena River (2013). In: In supplement to: Juhls, Bennet; Overduin, Pier Paul; Hölemann, Jens A;  
1290 Hieronymi, Martin; Matsuoka, Atsushi; Heim, Birgit; Fischer, Jürgen (2019): Dissolved organic matter at the fluvial–marine transition in the Laptev Sea using in situ data and ocean colour remote sensing. *Biogeosciences*, 16(13), 2693-2713, <https://doi.org/10.5194/bg-16-2693-2019>, PANGAEA, 2019.
- Lain, L. R., Kravitz, J., Matthews, M., and Bernard, S.: Simulated Inherent Optical Properties of Aquatic Particles using The Equivalent Algal Populations (EAP) model, *Scientific Data*, 10, 412, 10.1038/s41597-  
1295 023-02310-z, 2023.
- Le, C., Hu, C., English, D., Cannizzaro, J., Chen, Z., Kovach, C., Anastasiou, C. J., Zhao, J., and Carder, K. L.: Inherent and apparent optical properties of the complex estuarine waters of Tampa Bay: What controls light?, *Estuarine, Coastal and Shelf Science*, 117, 54-69, <https://doi.org/10.1016/j.ecss.2012.09.017>, 2013.
- 1300 Le, C., Lehrter, J. C., Hu, C., Schaeffer, B., MacIntyre, H., Hagy, J. D., and Beddick, D. L.: Relation between inherent optical properties and land use and land cover across Gulf Coast estuaries, *Limnol. Oceanogr.*, 60, 920-933, <https://doi.org/10.1002/lno.10065>, 2015.

Lee, Z., Carder, K. L., and Arnone, R. A.: Deriving inherent optical properties from water color: a  
multiband quasi-analytical algorithm for optically deep waters, *Applied Optics*, 41, 5755,  
1305 10.1364/AO.41.005755, 2002.

Lee, Z., Hu, C., Shang, S., Du, K., Lewis, M., Arnone, R., and Brewin, R.: Penetration of UV-visible  
solar radiation in the global oceans: Insights from ocean color remote sensing, *Journal of Geophysical  
Research: Oceans*, 118, 4241-4255, 10.1002/jgrc.20308, 2013.

Lee, Z. P., Du, K., Voss, K. J., Zibordi, G., Lubac, B., Arnone, R., and Weidemann, A.: An inherent-  
1310 optical-property-centered approach to correct the angular effects in water-leaving radiance, *Applied  
Optics*, 50, 3155, 10.1364/AO.50.003155, 2011.

Liu, Y., Wiegmann, S., and Bracher, A.: Absorption coefficient spectra (median) of non-algal particles  
during POLARSTERN cruise PS99. In: In supplement to: Liu, Yangyang; Boss, Emmanuel; Chase,  
Alison P; Xi, Hongyan; Zhang, Xiaodong; Röttgers, Rüdiger; Pan, Yanqun; Bracher, Astrid (2019):  
1315 Retrieval of phytoplankton pigments from underway spectrophotometry in the Fram Strait. *Remote  
Sensing*, 11(3), 318, <https://doi.org/10.3390/rs11030318>, PANGAEA, 2019a.

Liu, Y., Wiegmann, S., and Bracher, A.: Absorption coefficient spectra (median) of phytoplankton during  
POLARSTERN cruise PS99. In: In supplement to: Liu, Yangyang; Boss, Emmanuel; Chase, Alison P;  
Xi, Hongyan; Zhang, Xiaodong; Röttgers, Rüdiger; Pan, Yanqun; Bracher, Astrid (2019): Retrieval of  
1320 phytoplankton pigments from underway spectrophotometry in the Fram Strait. *Remote Sensing*, 11(3),  
318, <https://doi.org/10.3390/rs11030318>, PANGAEA, 2019b.

Liu, Y., Wiegmann, S., and Bracher, A.: Absorption coefficient spectra (median) of phytoplankton during  
POLARSTERN cruise PS107. In: In supplement to: Liu, Yangyang; Boss, Emmanuel; Chase, Alison P;  
Xi, Hongyan; Zhang, Xiaodong; Röttgers, Rüdiger; Pan, Yanqun; Bracher, Astrid (2019): Retrieval of  
1325 phytoplankton pigments from underway spectrophotometry in the Fram Strait. *Remote Sensing*, 11(3),  
318, <https://doi.org/10.3390/rs11030318>. In supplement to: Liu, Yangyang; Boss, Emmanuel; Chase,  
Alison P; Xi, Hongyan; Zhang, Xiaodong; Röttgers, Rüdiger; Pan, Yanqun; Bracher, Astrid (2019):



Retrieval of phytoplankton pigments from underway spectrophotometry in the Fram Strait. *Remote Sensing*, 11(3), 318, <https://doi.org/10.3390/rs11030318>, 2019c.

1330 Liu, Y., Wiegmann, S., and Bracher, A.: Absorption coefficient spectra (median) of non-algal particles during POLARSTERN cruise PS107. In: In supplement to: Liu, Yangyang; Boss, Emmanuel; Chase, Alison P; Xi, Hongyan; Zhang, Xiaodong; Röttgers, Rüdiger; Pan, Yanqun; Bracher, Astrid (2019): Retrieval of phytoplankton pigments from underway spectrophotometry in the Fram Strait. *Remote Sensing*, 11(3), 318, <https://doi.org/10.3390/rs11030318>, 2019d.

1335 Loisel, H., and Morel, A.: Light scattering and chlorophyll concentration in case 1 waters: A reexamination, *Limnol. Oceanogr.*, 43, 847-858, 10.4319/lo.1998.43.5.0847, 1998.

Loisel, H., and Morel, A.: Non-isotropy of the upward radiance field in typical coastal (Case 2) waters, *International Journal of Remote Sensing*, 22, 275-295, 10.1080/014311601449934, 2001.

1340 Loisel, H., Jorge, D. S. F., Reynolds, R. A., and Stramski, D.: A synthetic optical database generated by radiative transfer simulations in support of studies in ocean optics and optical remote sensing of the global ocean, *Earth Syst. Sci. Data*, 15, 3711-3731, 10.5194/essd-15-3711-2023, 2023.

Martinez-Vicente, V., Land, P. E., Tilstone, G. H., Widdicombe, C., and Fishwick, J. R.: Particulate scattering and backscattering related to water constituents and seasonal changes in the Western English Channel, *Journal of Plankton Research*, 32, 603-619, 10.1093/plankt/fbq013, 2010.

1345 Mason, J. D., Cone, M. T., and Fry, E. S.: Ultraviolet (250–550 nm) absorption spectrum of pure water, *Applied Optics*, 55, 7163-7172, 10.1364/AO.55.007163, 2016.

Massicotte, P., Babin, M., Fell, F., Fournier-Sicre, V., and Doxaran, D.: The Coastal Surveillance Through Observation of Ocean Color (COAST{OO}C) dataset, *Earth Syst. Sci. Data*, 15, 3529-3545, 10.5194/essd-15-3529-2023, 2023.

1350 Matthews, M. W., and Bernard, S.: Characterizing the Absorption Properties for Remote Sensing of Three Small Optically-Diverse South African Reservoirs, *Remote Sensing*, 5, 4370-4404, 2013.

Mobley, C. D., Gentili, B., Gordon, H. R., Jin, Z., Kattawar, G. W., Morel, A., Reinersman, P., Stamnes, K., and Stavn, R. H.: Comparison of numerical models for computing underwater light fields, *Applied Optics*, 32, 7484-7504, 10.1364/AO.32.007484, 1993.

1355 Mobley, C. D.: *Light and Water. Radiative Transfer in Natural Waters*, Academic Press, 1994.

Mobley, C. D., Sundman, L. K., and Boss, E.: Phase function effects on oceanic light fields, *Applied Optics*, 41, 1035, 10.1364/AO.41.001035, 2002.

Moradi, M., and Arabi, B.: Seasonal and spatial variability in bio-optical properties of the Persian Gulf: Implications for ocean color remote sensing, *Continental Shelf Research*, 266, 105094,

1360 <https://doi.org/10.1016/j.csr.2023.105094>, 2023.

Morel, A., and Gentili, B.: Diffuse reflectance of oceanic waters II Bidirectional aspects, *Applied Optics*, 32, 6864, 10.1364/AO.32.006864, 1993.

Morel, A., and Gentili, B.: Diffuse reflectance of oceanic waters III Implication of bidirectionality for the remote-sensing problem, *Applied Optics*, 35, 4850, 10.1364/AO.35.004850, 1996.

1365 Morel, A., and Maritorena, S.: Bio-optical properties of oceanic waters: A reappraisal, *Journal of Geophysical Research: Oceans*, 106, 7163-7180, 10.1029/2000JC000319, 2001.

Morel, A., Antoine, D., and Gentili, B.: Bidirectional reflectance of oceanic waters: accounting for Raman emission and varying particle scattering phase function, *Applied Optics*, 41, 6289, 10.1364/AO.41.006289, 2002.

1370 Morel, A.: Are the empirical relationships describing the bio-optical properties of case 1 waters consistent and internally compatible?, *Journal of Geophysical Research: Oceans*, 114, <https://doi.org/10.1029/2008JC004803>, 2009.

- Nechad, B., Ruddick, K., Schroeder, T., Oubelkheir, K., Blondeau-Patissier, D., Cherukuru, N., Brando, V., Dekker, A., Clementson, L., Banks, A. C., Maritorena, S., Werdell, P. J., Sá, C., Brotas, V., Caballero de Frutos, I., Ahn, Y. H., Salama, S., Tilstone, G., Martinez-Vicente, V., Foley, D., McKibben, M., Nahorniak, J., Peterson, T., Siliò-Calzada, A., Röttgers, R., Lee, Z., Peters, M., and Brockmann, C.: CoastColour Round Robin data sets: a database to evaluate the performance of algorithms for the retrieval of water quality parameters in coastal waters, *Earth Syst. Sci. Data*, 7, 319-348, 10.5194/essd-7-319-2015, 2015.
- 1375 Oubelkheir, K., Ford, P. W., Cherukuru, N., Clementson, L. A., Petus, C., Devlin, M., Schroeder, T., and Steven, A. D. L.: Impact of a Tropical Cyclone on Terrestrial Inputs and Bio-Optical Properties in Princess Charlotte Bay (Great Barrier Reef Lagoon), *Remote Sensing*, 15, 652, 2023.
- Park, Y.-J., and Ruddick, K.: Model of remote-sensing reflectance including bidirectional effects for case 1 and case 2 waters, *Applied Optics*, 44, 1236-1249, 10.1364/AO.44.001236, 2005.
- 1385 Petit, T., Hamre, B., Sandven, H., Röttgers, R., Kowalczuk, P., Zablocka, M., and Granskog, M. A.: Inherent optical properties of dissolved and particulate matter in an Arctic fjord (Storfjorden, Svalbard) in early summer, *Ocean Sci.*, 18, 455-468, 10.5194/os-18-455-2022, 2022.
- Pitarch, J., and Brando, V.: A hyperspectral and multi-angular synthetic dataset of optical properties for waters with varying trophic levels and optical complexity. Zenodo, 2024.
- 1390 Poulin, C., Zhang, X., Yang, P., and Huot, Y.: Diel variations of the attenuation, backscattering and absorption coefficients of four phytoplankton species and comparison with spherical, coated spherical and hexahedral particle optical models, *Journal of Quantitative Spectroscopy and Radiative Transfer*, 217, 288-304, <https://doi.org/10.1016/j.jqsrt.2018.05.035>, 2018.
- 1395 Pykäri, J.: Absorption measurements of colored dissolved organic matter (cDOM) in Pohjanpitäjänlahti bay in May 2021. In: In: Pykäri, J (2022): Light attenuation data set along a coastal salinity gradient in Pohjanpitäjänlahti bay in May 2021. PANGAEA, <https://doi.org/10.1594/PANGAEA.947091>, PANGAEA, 2022.

- Roettgers, R., McKee, D., and Utschig, C.: Temperature and salinity correction coefficients for light absorption by water in the visible to infrared spectral region, *Opt. Express*, 22, 25093-25108, 1400 10.1364/OE.22.025093, 2014.
- Roettgers, R., Doerffer, R., McKee, D., and Schonfeld, W.: Algorithm Theoretical Basis Document The Water Optical Properties Processor (WOPP). Pure water spectral absorption, scattering, and real part of refractive index model, Helmholtz-Zentrum Geesthacht, University of Strathclyde, ESA/ESRIN, 20, 2016.
- 1405 Rozanov, V. V., Rozanov, A. V., Kokhanovsky, A. A., and Burrows, J. P.: Radiative transfer through terrestrial atmosphere and ocean: Software package SCIATRAN, *Journal of Quantitative Spectroscopy and Radiative Transfer*, 133, 13-71, <https://doi.org/10.1016/j.jqsrt.2013.07.004>, 2014.
- Soppa, M. A., Dinter, T., Taylor, B. B., and Bracher, A.: Phytoplankton absorption during POLARSTERN cruise ANT-XXVIII/3. In: In supplement to: Soppa, MA et al. (2013): Satellite derived 1410 euphotic depth in the Southern Ocean: Implications for primary production modelling. *Remote Sensing of Environment*, 137, 198-211, <https://doi.org/10.1016/j.rse.2013.06.017>, PANGAEA, 2013a.
- Soppa, M. A., Dinter, T., Taylor, B. B., and Bracher, A.: Particulate absorption during POLARSTERN cruise ANT-XXVIII/3. In: In supplement to: Soppa, MA et al. (2013): Satellite derived euphotic depth in the Southern Ocean: Implications for primary production modelling. *Remote Sensing of Environment*, 1415 137, 198-211, <https://doi.org/10.1016/j.rse.2013.06.017>, PANGAEA, 2013b.
- Sullivan, J. M., and Twardowski, M. S.: Angular shape of the oceanic particulate volume scattering function in the backward direction, *Applied Optics*, 48, 6811, 10.1364/AO.48.006811, 2009.
- Szeto, M., Werdell, P. J., Moore, T. S., and Campbell, J. W.: Are the world's oceans optically different?, *Journal of Geophysical Research: Oceans*, 116, <https://doi.org/10.1029/2011JC007230>, 2011.

1420 Talone, M., Zibordi, G., and Pitarch, J.: On the Application of AERONET-OC Multispectral Data to Assess Satellite-Derived Hyperspectral Rrs, *IEEE Geosci. Remote Sensing Lett.*, 21, 1-5, 10.1109/LGRS.2024.3350928, 2024.

Tilstone, G. H., Peters, S. W. M., van der Woerd, H. J., Eleveld, M. A., Ruddick, K., Schönfeld, W., Krasemann, H., Martinez-Vicente, V., Blondeau-Patissier, D., Röttgers, R., Sørensen, K., Jørgensen, P.  
1425 V., and Shutler, J. D.: Variability in specific-absorption properties and their use in a semi-analytical ocean colour algorithm for MERIS in North Sea and Western English Channel Coastal Waters, *Remote Sensing of Environment*, 118, 320-338, <https://doi.org/10.1016/j.rse.2011.11.019>, 2012.

Twardowski, M. S., Boss, E., Macdonald, J. B., Pegau, W. S., Barnard, A. H., and Zaneveld, J. R. V.: A model for estimating bulk refractive index from the optical backscattering ratio and the implications for  
1430 understanding particle composition in case I and case II waters, *Journal of Geophysical Research: Oceans*, 106, 14129-14142, 10.1029/2000JC000404, 2001.

Valente, A., Sathyendranath, S., Brotas, V., Groom, S., Grant, M., Jackson, T., Chuprin, A., Taberner, M., Airs, R., Antoine, D., Arnone, R., Balch, W. M., Barker, K., Barlow, R., Bélanger, S., Berthon, J. F., Beşiktepe, Ş., Borsheim, Y., Bracher, A., Brando, V., Brewin, R. J. W., Canuti, E., Chavez, F. P., Cianca,  
1435 A., Claustre, H., Clementson, L., Crout, R., Ferreira, A., Freeman, S., Frouin, R., García-Soto, C., Gibb, S. W., Goericke, R., Gould, R., Guillocheau, N., Hooker, S. B., Hu, C., Kahru, M., Kappel, M., Klein, H., Kratzer, S., Kudela, R., Ledesma, J., Lohrenz, S., Loisel, H., Mannino, A., Martinez-Vicente, V., Matrai, P., McKee, D., Mitchell, B. G., Moisan, T., Montes, E., Muller-Karger, F., Neeley, A., Novak, M., O'Dowd, L., Ondrusek, M., Platt, T., Poulton, A. J., Repecaud, M., Röttgers, R., Schroeder, T., Smyth,  
1440 T., Smythe-Wright, D., Sosik, H. M., Thomas, C., Thomas, R., Tilstone, G., Tracana, A., Twardowski, M., Vellucci, V., Voss, K., Werdell, J., Wernand, M., Wojtasiewicz, B., Wright, S., and Zibordi, G.: A compilation of global bio-optical in situ data for ocean colour satellite applications – version three, *Earth Syst. Sci. Data*, 14, 5737-5770, 10.5194/essd-14-5737-2022, 2022.

- 1445 Vandermeulen, R. A., Mannino, A., Craig, S. E., and Werdell, P. J.: 150 shades of green: Using the full spectrum of remote sensing reflectance to elucidate color shifts in the ocean, *Remote Sensing of Environment*, 247, 111900, <https://doi.org/10.1016/j.rse.2020.111900>, 2020.
- Werdell, P. J., and Bailey, S. W.: An improved in-situ bio-optical data set for ocean color algorithm development and satellite data product validation, *Remote Sensing of Environment*, 98, 122-140, <https://doi.org/10.1016/j.rse.2005.07.001>, 2005.
- 1450 Whitmire, A. L., Pegau, W. S., Karp-Boss, L., Boss, E., and Cowles, T. J.: Spectral backscattering properties of marine phytoplankton cultures, *Opt. Express*, 18, 15073-15093, 10.1364/OE.18.015073, 2010.
- Wiegmann, S., Liu, Y., and Bracher, A.: Absorption coefficient spectra (median) of non-algal particles during POLARSTERN cruise PS93.2. In: In supplement to: Liu, Yangyang; Boss, Emmanuel; Chase, Alison P; Xi, Hongyan; Zhang, Xiaodong; Röttgers, Rüdiger; Pan, Yanqun; Bracher, Astrid (2019): Retrieval of phytoplankton pigments from underway spectrophotometry in the Fram Strait. *Remote Sensing*, 11(3), 318, <https://doi.org/10.3390/rs11030318>, PANGAEA, 2019.
- Zhang, X., and Hu, L.: Light Scattering by Pure Water and Seawater: Recent Development, *Journal of Remote Sensing*, 2021, doi:10.34133/2021/9753625, 2021.
- 1460 Zibordi, G., and Berthon, J. F.: Coastal Atmosphere & Sea Time Series (CoASTS) and Bio-Optical mapping of Marine optical Properties (BiOMaP): the CoASTS-BiOMaP dataset, *Earth Syst. Sci. Data Discuss.*, 2024, 1-33, 10.5194/essd-2024-240, 2024.